



1 **Global scale variability of the mineral dust longwave refractive index:**
2 **a new dataset of in situ measurements for climate modelling and remote sensing**

3
4 Claudia Di Biagio¹, Paola Formenti¹, Yves Balkanski², Lorenzo Caponi^{1,3}, Mathieu Cazaunau¹, Edou-
5 ard Panguì¹, Emilie Journet¹, Sophie Nowak⁴, Sandrine Caquineau⁵, Meinrat O. Andreae^{6,12}, Konrad
6 Kandler⁷, Thuraya Saeed⁸, Stuart Piketh⁹, David Seibert¹⁰,
7 Earle Williams¹¹, and Jean-Francois Doussin¹

8
9 ¹ *Laboratoire Interuniversitaire des Systèmes Atmosphériques (LISA), UMR 7583, CNRS, Université Paris Est*
10 *Créteil et Université Paris Diderot, Institut Pierre et Simon Laplace, Créteil, France*

11 ² *Laboratoire des Sciences du Climat et de l'Environnement, CEA CNRS UVSQ, 91191, Gif sur Yvette, France*

12 ³ *University of Genoa, Genoa, Italy*

13 ⁴ *Plateforme RX UFR de chimie, Université Paris Diderot, Paris, France*

14 ⁵ *IRD-Sorbonne Universités (UPMC, Univ. Paris 06) – CNRS-MNHN, LOCEAN Laboratory, IRD France-Nord,*
15 *F-93143 Bondy, France*

16 ⁶ *Biogeochemistry Department, Max Planck Institute for Chemistry, P.O. Box 3060, 55020, Mainz, Germany*

17 ⁷ *Institut für Angewandte Geowissenschaften, Technische Universität Darmstadt, Schnittspahnstr. 9, 64287*
18 *Darmstadt, Germany*

19 ⁸ *Science department, College of Basic Education, Public Authority for Applied Education and Training, Al-*
20 *Ardeya, Kuwait*

21 ⁹ *Climatology Research Group, Unit for Environmental Science and Management, North-West University,*
22 *Potchefstroom, South Africa*

23 ¹⁰ *Walden University, Minneapolis, Minnesota, USA*

24 ¹¹ *Parsons Laboratory, Massachusetts Institute of Technology, Cambridge, Massachusetts, USA*

25 ¹² *Department of Geosciences, King Saud University, Riyadh, Saudi Arabia*

26

27

28

29

30 Correspondence to:

31 C. Di Biagio (claudia.dibiagio@lisa.u-pec.fr) and P. Formenti (paola.formenti@lisa.u-pec.fr)

32



33 **Abstract**

34 Modelling the interaction of dust with longwave (LW) radiation is still a challenge due to the scarcity
35 of information on the complex refractive index of dust from different source regions. In particular,
36 little is known on the variability of the refractive index as a function of the dust mineralogical compo-
37 sition, depending on the source region of emission, and the dust size distribution, which is modified
38 during transport. As a consequence, to date, climate models and remote sensing retrievals generally
39 use a spatially-invariant and time-constant value for the dust LW refractive index.

40 In this paper the variability of the mineral dust LW refractive index as a function of its mineralogical
41 composition and size distribution is explored by in situ measurements in a large smog chamber. Min-
42 eral dust aerosols were generated from nineteen natural soils from Northern Africa, Sahel, Middle
43 East, Eastern Asia, North and South America, Southern Africa, and Australia. Soil samples were se-
44 lected from a total of 137 samples available in order to represent the diversity of sources from arid and
45 semi-arid areas worldwide and to account for the heterogeneity of the soil composition at the global
46 scale. Aerosol samples generated from soils were re-suspended in the chamber, where their LW extinc-
47 tion spectra (2-16 μm), size distribution, and mineralogical composition were measured. The generated
48 aerosol exhibits a realistic size distribution and mineralogy, including both the sub- and super-micron
49 fractions, and represents in typical atmospheric proportions the main LW-active minerals, such as
50 clays, quartz, and calcite. The complex refractive index of the aerosol is obtained by an optical inver-
51 sion based upon the measured extinction spectrum and size distribution.

52 Results from the present study show that the LW refractive index of dust varies greatly both in magni-
53 tude and spectral shape from sample to sample, following the changes in the measured particle compo-
54 sition. The real part (n) of the refractive index is between 0.84 and 1.94, while the imaginary part (k) is
55 ~ 0.001 and 0.92. For instance, the strength of the absorption at ~ 7 and 11.4 μm depends on the amount
56 of calcite within the samples, while the absorption between 8 and 14 μm is determined by the relative
57 abundance of quartz and clays. A linear relationship between the magnitude of the refractive index at
58 7.0, 9.2, and 11.4 μm and the mass concentration of calcite and quartz absorbing at these wavelengths
59 was found. We suggest that this may lead to predictive rules to estimate the LW refractive index of
60 dust in specific bands based on an assumed or predicted mineralogical composition, or conversely, to
61 estimate the dust composition from measurements of the LW extinction at specific wavebands.



62 Based on the results of the present study, we recommend using refractive indices specific for the dif-
63 ferent source regions, rather than generic values, in climate models and remote sensing applications.
64 Our observations also suggest that the refractive index of dust in the LW does not change due to the
65 loss of coarse particles by gravitational settling, so that a constant value could be assumed close to
66 sources and during transport. The results of the present study also clearly suggest that the LW refrac-
67 tive index of dust varies at the regional scale. This regional variability has to be characterized further
68 in order to better assess the influence of dust on regional climate, as well as to increase the accuracy of
69 satellite retrievals over regions affected by dust.

70 We make the whole dataset of the dust complex refractive indices obtained here available to the scien-
71 tific community by publishing it in the supplementary material to this paper.

72

73 **Keywords:** mineral dust, longwave refractive index, mineralogy, size distribution, global variability

74

75

76 1. Introduction

77 Mineral dust is one of the most abundant aerosol species in the atmosphere and contributes significant-
78 ly to radiative perturbation, both at the regional and the global scale (Miller et al., 2014). The direct
79 radiative effect of mineral dust acts both at shortwave (SW) and longwave (LW) wavelengths (Tegen
80 and Lacis, 1996). This is due to the very large size spectrum of these particles, which extends from
81 hundreds of nanometers to tenths of micrometers, and to their mineralogy, which includes minerals
82 with absorption bands at both SW and LW wavelengths (Sokolik et al., 1998; Sokolik and Toon,
83 1999). The sub-micron dust fraction controls the interaction in the SW, where scattering is the domi-
84 nant process, while the super-micron size fraction drives the LW interaction, dominated by absorption
85 (Sokolik and Toon, 1996 and 1999). The SW and LW terms have opposite effects at the surface, Top-
86 of-Atmosphere (TOA), and within the atmosphere (Hsu et al., 2000). Indeed, the dust SW effect is to
87 cool the surface and the TOA, and to warm the atmosphere; conversely, the dust LW effect induces a
88 warming of the surface and TOA, and an atmospheric cooling.

89 The interaction of dust with LW radiation has key implications for climate modelling and remote sens-
90 ing. Many studies have shown the key role of the LW effect in modulating the SW perturbation of dust



91 not only close to sources (Slingo et al., 2006), where the coarse size fraction is dominant (Schütz et al.,
92 1974; Ryder et al., 2013a), but also after medium- and long- range transport (di Sarra et al., 2011;
93 Meloni et al., 2015), when the larger particles ($> 10 \mu\text{m}$) were preferentially removed by wet and dry
94 deposition (Schütz et al., 1981; Maring et al., 2003; Osada et al., 2014). Thus, the dust LW term has
95 importance over the entire dust lifecycle, and has to be taken into account in order to evaluate the radi-
96 ative effect of dust particles on the climate system. Second, the signature of the dust LW absorption
97 modifies the TOA radiance spectrum, which influences the retrieval of several climate parameters by
98 satellite remote sensing. Misinterpretations of the data may occur if the signal of dust is not accurately
99 taken into account within satellite inversion algorithms (Sokolik, 2002; DeSouza-Machado et al.,
100 2006; Maddy et al., 2012). In addition, the dust LW signature obtained by spaceborne satellite data in
101 the 8–12 μm window region is used to estimate the concentration fields and optical depth of dust (Klü-
102 ser et al., 2011; Capelle et al., 2014; Cuesta et al., 2015), with potential important applications for cli-
103 mate and air quality studies, health issues, and visibility.

104 Currently, the magnitude and the spectral fingerprints of the dust signal in the LW are still very uncer-
105 tain. The highest uncertainty comes from the poor knowledge on the dust spectral complex refractive
106 index ($m = n - ik$) (Claquin et al., 1998; Liao and Seinfeld, 1998; Sokolik et al., 1998; Highwood et al.,
107 2003; Colarco et al., 2014). The dust complex refractive index in the LW depends on the particle min-
108 eralogical composition, in particular the relative proportion of quartz, clays (kaolinite, illite, smectite,
109 chlorite), and calcium-rich minerals (calcite, dolomite), each exhibiting specific absorption features in
110 the LW spectrum (Sokolik et al., 1993 and 1998). Because of the variability of the dust composition
111 resulting from the variability of composition of the source soils (Jeong, 2008; Scheuven et al., 2013;
112 Formenti et al., 2014; Journet et al., 2014), atmospheric dust produced from different regions of the
113 world is expected to have a varying complex refractive index. Additional variability is expected to be
114 introduced during transport due to the progressive loss of coarse particles by gravitational settling and
115 processing, which both change the mineralogical composition (Pye et al., 1987; Usher et al., 2003). As
116 a consequence, the refractive index of dust is expected to vary widely at the regional and global scale.

117 Several studies have recommended taking into account the variability of the dust LW refractive index
118 in order to correctly represent its effect in climate models and satellite retrieval algorithms (Sokolik et
119 al., 1998; Claquin et al., 1999; Balkanski et al., 2007; Colarco et al., 2014; Capelle et al., 2014; among
120 others). However, to date this is precluded by the limited body of observations available. Most past
121 studies on the LW refractive index have been performed on single synthetic minerals (see Table 1 in



122 Otto et al., 2009). These data, however, are not adequate to reproduce atmospheric dust because of the
123 chemical differences between the reference minerals and the minerals in the natural aerosol, and also
124 because of the difficulty of effectively evaluating the refractive index of the dust aerosol based only on
125 information on its single constituents (e.g., McConnell et al., 2010). On the other hand, very few stud-
126 ies have been performed on natural aerosol samples. They include the estimates obtained with the KBr
127 pellet technique by Volz (1972, 1973), Fouquart (1987), and, more recently, by Di Biagio et al.
128 (2014a), on dust samples collected at a few geographical locations (Germany, Barbados, Niger, and
129 Algeria). Besides hardly representing global dust sources, these datasets are also difficult to extrap-
130 olate to atmospheric conditions as (i) they mostly refer to unknown dust mineralogical composition and
131 size distribution, and also (ii) are obtained from analyses of field samples that might have experienced
132 unknown physico-chemical transformations. In addition, they have a rather coarse spectral resolution,
133 which is sometimes insufficient to resolve the main dust spectral features.

134 As a consequence, climate models and satellite retrievals presently use a spatially-invariant and time-
135 constant value for the dust LW refractive index (e.g., Miller et al., 2014; Capelle et al., 2014), implicit-
136 ly assuming a uniform as well as transport- and processing-invariant dust composition.

137 Recently, novel data of the LW refractive index for dust from the Sahara, the Sahel, and the Gobi de-
138 serts have been obtained from in situ measurements in a large smog chamber (Di Biagio et al., 2014b;
139 hereinafter DB14). These measurements were performed in the realistic and dynamic environment of
140 the 4.2 m³ CESAM chamber (French acronym for Experimental Multiphasic Atmospheric Simulation
141 Chamber) (Wang et al., 2011), using a validated generation mechanism to produce mineral dust from
142 parent soils (Alfaro et al., 2004). The mineralogical composition and size distribution of the particles
143 were measured along with the optical data, thus providing a link between particle physico-chemical
144 and optical properties.

145 In this study, we review, optimize, and extend the approach of DB14 to investigate the LW optical
146 properties of mineral dust aerosols from nineteen soils from major source regions worldwide, in order
147 to: (i) characterize the dependence of the dust LW refractive index on the particle origin and different
148 mineralogical compositions; and (ii) investigate the variability of the refractive index as a function of
149 the change in size distribution that may occur during medium- and long-range transport.

150 The paper is organized as follows: in Sect. 2 we describe the experimental set-up, instrumentation and
151 data analysis, while in Sect. 3 the algorithm to retrieve the LW complex refractive index from observa-



152 tions is discussed. Criteria for soil selection and their representativeness of the global dust are dis-
153 cussed in Sect. 4. Results are presented in Sect. 5. At first, the atmospheric representativeness in terms
154 of mineralogy and size distribution of the generated aerosols used in the experiments is evaluated
155 (Sect. 5.1 and 5.2), then the extinction and complex refractive index spectra obtained for the different
156 source regions and at different aging times in the chamber are presented in Sect. 5.3. The discussion of
157 the results, their comparison with the literature, and the main conclusions are given in Sect. 6 and 7.

158

159 2. Experimental set-up and instrumentation

160 The schematic configuration of the CESAM chamber set-up for the dust experiments is shown in Fig.
161 1. Prior to each experiment, the chamber was evacuated and kept at a pressure of $3 \cdot 10^{-4}$ hPa. Then, the
162 reactor was filled with a mixture of 80% N₂ (produced by evaporation from a pressurized liquid nitro-
163 gen tank, Messer, purity >99.995%) and 20% O₂ (Linde, 5.0). The chamber was equipped with a four-
164 blade stainless steel fan to achieve homogeneous conditions within the chamber volume (with a typical
165 mixing time of approximately 1 minute). Mineral dust aerosols generated from parent soils were dis-
166 persed into the chamber and left in suspension for a time period of 60-120 min, whilst monitoring the
167 evolution of their physico-chemical and optical properties. The LW spectrum of the dust aerosols was
168 measured by means of an in situ FTIR. Concurrently, the particle size distribution and the SW scatter-
169 ing and absorption coefficients were measured by several instruments sampling aerosols from the
170 chamber. They include a scanning mobility particle sizer (SMPS), and WELAS and SkyGrimm optical
171 particle counters for the size distribution, and a nephelometer (TSI Inc. model 3563), an aethalometer
172 (Magee Sci. model AE31), and two Cavity Attenuated Phase Shift Extinction (CAPS PMeX by Aero-
173 dyne) for aerosol SW optical properties. Dust samples were also collected over the largest part of each
174 experiment on polycarbonate filters (47-mm Nuclepore, Whatman, nominal pore size 0.4 μm) for an
175 analysis of the particle mineralogical composition averaged over the length of the experiment.

176 Inlets for the instruments sampling aerosols from the chamber (size, SW optics, filter sampling) con-
177 sisted of two parts: 1) a stainless steel tube (~20-40 cm length, 9.5 mm diameter) located inside
178 CESAM which extracted air from the interior of the chamber and 2) an external connection from the
179 chamber to the instruments. All external connections were made using 0.64 cm conductive silicone
180 tubing (TSI Inc.) that minimizes particle loss by electrostatic deposition. The sampling lines were de-
181 signed to be as straight and as short as possible, and their total length varied between 40 and 120 cm.



182 The possible losses as a function of particle diameter were carefully estimated for each inlet and the
183 related data properly corrected (Sect. 2.3.2). To compensate for the air being extracted from the cham-
184 ber by the various instruments, a particle-free N₂/O₂ mixture was continuously injected into the cham-
185 ber.

186 All experiments were conducted at ambient temperature and relative humidity <2%. The chamber was
187 manually cleaned between the different experiments to avoid any carryover contaminations as far as
188 possible. Background concentrations of aerosols in the chamber varied between 0.5 and 2.0 µg m⁻³.

189 In the following paragraphs we describe the system for dust generation, measurements of dust LW
190 spectrum, size distribution, and mineralogy, and data analysis. A summary of the different measured
191 and retrieved quantities in this study and their estimated uncertainties is reported in Table 1. Longwave
192 optical and size distribution data, acquired with different temporal resolutions, are averaged over 10-
193 min intervals. Uncertainties on the average values are obtained as the standard deviation over the 10-
194 min intervals.

195 A full description of the SW optical measurements and results is out of the scope of the present study
196 and will be provided in a forthcoming paper (Di Biagio et al., in preparation).

197

198 **2.1 Dust aerosol generation**

199 In order to mimic the natural emission process, dust aerosols were generated by mechanical shaking of
200 natural soil samples as described in DB14. The soils used in this study consist of the surface layer,
201 which is subject to wind erosion in nature (Pye et al., 1987). Prior to each experiment, the soil samples
202 were sieved to <1000 µm and dried at 100 °C for about 1 h to remove any residual humidity. This pro-
203 cessing did not affect the mineral crystalline structure of the soil (Sertsu and Sánchez, 1978).

204 About 15 g of soil sample was placed in a Büchner flask and shaken for about 30 min at 100 Hz by
205 means of a sieve shaker (Retsch AS200). The dust suspension in the flask was then injected into the
206 chamber by flushing it with N₂ at 10 L min⁻¹ for about 10-15 min, whilst continuously shaking the soil.
207 Larger quantities of soil sample (60 g) mixed with pure quartz (60 g) had been used in DB14 to max-
208 imize the concentrations of the generated dust. The presence of the pure quartz grains increases the
209 efficiency of the shaking, allowing a rapid generation of high dust concentrations. In that case it had
210 been necessary, however, to pass the aerosol flow through a stainless steel settling cylinder to avoid



211 large quartz grains from entering the chamber (DB14). For the present experiments the generation sys-
212 tem was optimized, i.e. the mechanical system used to fix the flask to the shaker was improved so that
213 the soil shaking was more powerful, and sufficient quantities of dust aerosols could be generated by
214 using a smaller amount of soil and without adding quartz to the soil sample. In this way, the settling
215 cylinder could be eliminated. No differences were observed in the size distribution or mineralogy of
216 the generated dust between the two approaches.

217

218 **2.2 LW optical measurements: FTIR extinction spectrum**

219 The extinction spectrum of dust aerosols in the longwave was measured by means of an in situ Fourier
220 Transform Infrared spectrometer (FTIR) (Bruker® Tensor 37™) analytical system. The spectrometer
221 is equipped with a liquid nitrogen-cooled Mercury Cadmium Telluride (MCT) detector and a Global
222 source. The FTIR measures between wavelengths of 2.0 μm (5000 cm⁻¹) and 16 μm (625 cm⁻¹) at 2
223 cm⁻¹ resolution by co-adding 158 scans over 2 minutes. The FTIR is interfaced with a multi-pass cell
224 to achieve a total optical path length (x) within the chamber of 192 ± 4 m. The FTIR reference spec-
225 trum was acquired immediately before the dust injection. In some cases small amounts of water vapor
226 and CO₂ entered CESAM during particle injection and partly contaminated the dust spectra below 7
227 μm. This did not influence the state of particles as the chamber remained very dry (relative humidity <
228 2%). Water vapor and CO₂ absorption lines were carefully subtracted using reference spectra. The
229 measured spectra were then interpolated at 0.02 μm wavelength resolution. Starting from the FTIR
230 measured transmission (T), the dust spectral extinction coefficient β_{ext} in the 2-16 μm range was calcu-
231 lated as:

$$232 \quad \beta_{\text{ext}}(\lambda) = \frac{-\ln(T(\lambda))}{x}. \quad (1)$$

233 The uncertainty on β_{ext} was calculated with the error propagation formula by considering the uncertain-
234 ties arising from T noise (~1%) and from the standard deviation of the 10-min averages and of the path
235 length x . We estimated it to be ~10%.

236 In the 2-16 μm range the dust extinction measured by the FTIR is due to the sum of scattering and ab-
237 sorption. Scattering dominates below 6 μm, while absorption is dominant above 6 μm. The FTIR mul-
238 tipass cell in the CESAM chamber has been built following the White (1942) design (see Fig. 1). In
239 this configuration, a significant fraction of the light scattered by the dust enters the FTIR detector and



240 is not measured as extinction. This is because mineral dust is dominated by the super-micron fraction,
241 which scatters predominantly in the forward direction. As a consequence, the FTIR signal in the pres-
242 ence of mineral dust will represent only a fraction of dust scattering below 6 μm and almost exclusive-
243 ly absorption above 6 μm . Figure S1 (supplementary material), shows an example of the angular dis-
244 tribution of scattered light (phase function) and the scattering-to-absorption ratio calculated as a func-
245 tion of the wavelength in the LW for one of the samples used in this study. Results of the calculations
246 confirm that above 6 μm the scattering signal measured by the FTIR accounts for less than 20% of the
247 total LW extinction at the peak of the injection and less than 10% after 120 minutes in the chamber.
248 Consequently, we approximate Eq. (1) as:

$$249 \quad \beta_{\text{abs}}(\lambda) \approx \frac{-\ln(T(\lambda))}{x} \quad (\lambda > 6 \mu\text{m}). \quad (2)$$

250

251 **2.3 Size distribution measurements**

252 The particle number size distribution in the chamber was measured with several instruments based on
253 different principles and operating in different size ranges:

- 254 - a scanning mobility particle sizer (SMPS) (TSI, DMA Model 3080, CPC Model 3772; operated at
255 2.0/0.2 L min^{-1} sheath/aerosol flow rates; 2-min resolution) measuring the dust electrical mobili-
256 ty diameters (D_m , i.e., the diameter of a sphere with the same migration velocity in a constant
257 electric field as the particle of interest) in the range 0.019–0.882 μm . Given that dust particles
258 have a density larger than unity (assuming an effective density of 2.5 g cm^{-3}), the cut point of the
259 impactor at the input of the SMPS shifts towards lower diameters. This reduces the range of
260 measured mobility diameters to \sim 0.019–0.50 μm . The SMPS was calibrated prior the campaign
261 with PSL particles (Thermo Sci.) of 0.05, 0.1, and 0.5 μm nominal diameters;
- 262 - a WELAS optical particle counter (PALAS, model 2000; white light source between 0.35–0.70 μm ;
263 flow rate 2 L min^{-1} ; 1-min resolution) measuring the dust sphere-equivalent optical diameters
264 (D_{opt} , i.e., the diameter of a sphere yielding on the same detector geometry the same optical re-
265 sponse as the particle of interest) in the range 0.58–40.7 μm . The WELAS was calibrated prior
266 the campaign with Caldust 1100 (Palas) reference particles;



267 - a SkyGrimm optical particle counter (Grimm Inc., model 1.129; 0.655 μm operating wavelength;
268 flow rate 1.2 L min^{-1} ; 6-sec resolution) measuring the dust sphere-equivalent optical diameters
269 (D_{opt}) in the range 0.25-32 μm . The SkyGrimm was calibrated after the campaign against a
270 “master” Grimm (model 1.109) just recalibrated at the factory.

271 The SMPS and the WELAS were installed at the bottom of the chamber, while the SkyGrimm was
272 installed at the top of the chamber on the same horizontal plane as the FTIR spectrometer and at about
273 60 cm across the chamber from the WELAS and the SMPS. As already discussed in DB14, measure-
274 ments at the top and bottom of the chamber are in very good agreement during the whole duration of
275 each experiment, which indicates a good homogeneity of the dust aerosols in the chamber.

276

277 2.3.1 Corrections of SMPS, WELAS, and SkyGrimm data

278 Different corrections have to be applied to the instruments measuring the particle size distribution. For
279 the SMPS, corrections for particle loss by diffusion in the instrument tubing and the contribution of
280 multiple-charged particles were performed using the SMPS software. The electrical mobility diameter
281 measured by the SMPS was converted to a geometrical diameter (D_g) by taking into account the parti-
282 cle dynamic shape factor (χ), as $D_g = D_m / \chi$. The shape factor χ , determined by comparison with the
283 SkyGrimm in the overlapping particle range (~ 0.25 - $0.50 \mu\text{m}$), was found to be 1.75 ± 0.10 . This value
284 is higher than those reported in the literature for mineral dust (1.1-1.6; e.g., Davies, 1979; Kaaden et
285 al., 2008). The uncertainty in D_g was estimated with the error propagation formula and was $\sim 6\%$.

286 For the WELAS, optical diameters were converted to sphere-equivalent geometrical diameters (D_g) by
287 taking into account the visible complex refractive index. The D_{opt} to D_g diameter conversion was per-
288 formed based on the range of values reported in the literature for dust in the visible range, i.e., 1.47–
289 1.53 for the real part and 0.001–0.005 for the imaginary part (Osborne et al., 2008; Otto et al., 2009;
290 McConnell et al., 2010; Kim et al., 2011; Klaver et al., 2011). Optical calculations were computed
291 over the spectral range of the WELAS using Mie theory for spherical particles by fixing n at 1.47, 1.50
292 and 1.53 and by varying k in steps of 0.001 between 0.001 and 0.005. The spectrum of the WELAS
293 lamp needed for optical calculations was measured in the laboratory (Fig. S2, supplementary material).
294 D_g was then set at the mean \pm one standard deviation of the values obtained for the different n and k .
295 After calculations, the WELAS D_g range became 0.65-73.0 μm with an associated uncertainty of $<5\%$



296 for $D_g < 10 \mu\text{m}$ and between 5 and 7% at larger diameters. A very low counting efficiency was observed
 297 for the WELAS below $1 \mu\text{m}$, thus data in this size range were discarded.

298 For the SkyGrimm, the D_{opt} to D_g diameter conversion was performed with a procedure similar to that
 299 used for the WELAS. After calculations, the D_g range for the SkyGrimm became $0.29\text{--}68.2 \mu\text{m}$ with
 300 an associated uncertainty $< 15.2\%$ at all diameters. The inter-calibration between the SkyGrimm and
 301 the master instrument showed a relatively good agreement ($< 20\%$ difference in particle number) at
 302 $D_g < 1 \mu\text{m}$, but a large disagreement (up to 300% difference) at $D_g > 1 \mu\text{m}$. Based on inter-comparison
 303 data, a recalibration curve was calculated for the SkyGrimm in the range $D_g < 1 \mu\text{m}$, and the data for
 304 $D_g > 1 \mu\text{m}$ were discarded. The SkyGrimm particle concentration was also corrected for the flow rate of
 305 the instrument, which during the experiment was observed to vary between 0.7 and 1.2 L min^{-1} com-
 306 pared to its nominal value at 1.2 L min^{-1} .

307

308 **2.3.2 Correction for particle losses in sampling lines and determination of the full dust size dis-** 309 **tribution at the input of each instrument**

310 In order to compare and combine extractive measurements (size distribution, filter sampling, and SW
 311 optics), particle losses due to aspiration and transmission in the sampling lines were calculated using
 312 the Particle Loss Calculator (PLC) software (von der Weiden et al., 2009). Inputs to the software in-
 313 clude the geometry of the sampling line, the sampling flow rate, the particle shape factor χ , and the
 314 particle density (set at 2.5 g cm^{-3} for dust).

315 Particle losses for the instruments measuring the number size distribution (SMPS, WELAS, and
 316 SkyGrimm) were calculated. This allowed reconstructing the dust size distribution suspended in the
 317 CESAM chamber that corresponds to the size distribution sensed by the FTIR and that is needed for
 318 optical calculations in the LW. Particle loss was found negligible at $D_g < 1 \mu\text{m}$, reaching 50% at $D_g \sim 5$
 319 μm , 75% at $D_g \sim 6.3 \mu\text{m}$, and 95% at $D_g \sim 8 \mu\text{m}$ for the WELAS, the only instrument considered in the
 320 super-micron range. Data for the WELAS were then corrected as

$$321 \quad \left[\frac{dN}{d \log D_g} \right]_{\text{Corr, WELAS}} = \left[\frac{dN}{d \log D_g} \right]_{\text{WELAS}} / \left[1 - L_{\text{WELAS}}(D_g) \right] \quad (3)$$

322 where $[dN/d \log D_g]_{\text{WELAS}}$ is the size measured by the WELAS and $L_{\text{WELAS}}(D_g)$ is the calculated particle
 323 loss as a function of the particle diameter. Data at $D_g > 8 \mu\text{m}$, for which the loss is higher than 95%,
 324 were excluded from the dataset due to their large uncertainty. The uncertainty on $L_{\text{WELAS}}(D_g)$ was es-



325 timated with a sensitivity study by varying the PLC software values of the input parameters within
 326 their error bars. The $L_{\text{WELAS}}(D_g)$ uncertainty varies between $\sim 50\%$ at $2 \mu\text{m}$ to $\sim 10\%$ at $8 \mu\text{m}$. The total
 327 uncertainty in the WELAS-corrected size distribution was estimated as the combination of the
 328 $dN/d\log D_g$ standard deviation on the 10-min average and the $L_{\text{WELAS}}(D_g)$ uncertainty.

329 The full size distribution of dust aerosols within the CESAM chamber $[dN/d\log D_g]_{\text{CESAM}}$ was deter-
 330 mined by combining SMPS and SkyGrimm data with WELAS loss-corrected data: the SMPS was tak-
 331 en at $D_g < 0.3 \mu\text{m}$, the SkyGrimm at $D_g = 0.3\text{--}1.0 \mu\text{m}$, and the WELAS at $D_g = 1.0\text{--}8.0 \mu\text{m}$. Data were then
 332 interpolated in steps of $d\log D_g = 0.05$. An example of the size distributions measured by the different
 333 instruments is shown in Fig. S3 in the supplement for this paper. Above $8 \mu\text{m}$, where WELAS data
 334 were not available, the dust size distribution was extrapolated by applying a single-mode lognormal fit.
 335 The fit was set to reproduce the shape of the WELAS distribution between $D_g \sim 3\text{--}4$ and $8 \mu\text{m}$.

336 Particle losses in the filter sampling system ($L_{\text{filter}}(D_g)$) were calculated estimating the size-dependent
 337 particles losses that would be experienced by an aerosol with the size distribution in CESAM recon-
 338 structed from the previous calculations. Losses for the sampling filter were negligible for $D_g < 1 \mu\text{m}$,
 339 and increased to 50% at $D_g \sim 6.5 \mu\text{m}$, 75% at $D_g \sim 9 \mu\text{m}$, and 95% at $D_g \sim 12 \mu\text{m}$. The loss function,
 340 $L_{\text{filter}}(D_g)$, was used to estimate the dust size distribution at the input of the filter sampling system as

$$341 \quad [dN/d\log D_g]_{\text{filter}} = [dN/d\log D_g]_{\text{CESAM}} * [1 - L_{\text{filter}}(D_g)] \quad (4).$$

342 As a consequence of losses, the FTIR and the filters sense particles over different size ranges. Figure
 343 S4 (supplementary material) illustrates this point by showing a comparison of the calculated size dis-
 344 tribution within CESAM and that sampled on filters for one typical case. An underestimation of the
 345 particle number on the sampling filter compared to that measured in CESAM is observed above $10 \mu\text{m}$
 346 diameter. While the filter samples would underestimate the mass concentration in the chamber, the
 347 relative proportions of the main minerals should be well represented. As a matter of fact, at emission,
 348 where particles of diameters above $10 \mu\text{m}$ are most relevant, the mineralogical composition in the 10--
 349 $20 \mu\text{m}$ size class matches that of particles of diameters between 5 and $10 \mu\text{m}$ (Kandler et al., 2009).
 350 When averaging, and also taking into account the contribution of the mass of the $10\text{--}20 \mu\text{m}$ size class
 351 to the total, differences in the relative proportions of minerals do not exceed 10% .

352

353



354 2.4 Analysis of the dust aerosol mineralogical composition

355 The mineralogical composition of the aerosol particles collected on the filters was determined by X-
356 Ray Diffraction (XRD) analysis. XRD analysis was performed using a Panalytical model Empyrean
357 diffractometer with Ni-filtered $\text{CuK}\alpha$ radiation at 45 kV and 40 mA. Samples were scanned from 5 to
358 60° (2θ) in steps of 0.026° , with a time per step of 200 s. Samples were prepared and analyzed accord-
359 ing to the protocols of Caquineau et al. (1997) for low mass loadings (load deposited on filter <800
360 μg). Particles were first extracted from the filter with ethanol, then concentrated by centrifuging
361 ($25,000$ rpm for 30 min), diluted with deionized water ($\text{pH} \sim 7.1$), and finally deposited on a pure sili-
362 con slide.

363 For well-crystallized minerals, such as quartz, calcite, dolomite, gypsum and feldspars (orthoclase,
364 albite), a mass calibration was performed in order to establish the relationship between the intensity of
365 the diffraction peak and the mass concentration in the aerosol samples, according to the procedure de-
366 scribed in Klaver et al. (2011). The calibration coefficients K_i , representing the ratio between the total
367 peak surface area in the diffraction spectra (S_i) and the mass m_i of the i^{th} -mineral, are reported in Table
368 S1 in the supplementary material. The error in the obtained mass of each mineral was estimated with
369 the error propagation formula taking into account the uncertainty in S_i and the calibration coefficients
370 K_i . The obtained uncertainty is $\pm 9\%$ for quartz, $\pm 14\%$ for orthoclase, $\pm 8\%$ for albite, $\pm 11\%$ for calcite,
371 $\pm 10\%$ for dolomite, and $\pm 18\%$ for gypsum.

372 Conversely, the mass concentration of clays (kaolinite, illite, smectite, palygorskite, chlorite), also de-
373 tected in the samples, cannot be quantified in absolute terms from the XRD spectra due to the absence
374 of appropriate calibration standards for these components (Formenti et al., 2014). Hence, the total clay
375 mass was estimated as the difference between the total dust mass calculated from particle size distribu-
376 tion $\left[\frac{dN}{d \log D_g} \right]_{\text{filter}}$ and the total mass of quartz, calcium-rich species, and feldspars estimated after
377 calibration. The mass of organic material was neglected, as well as that of iron and titanium oxides,
378 whose contributions should not exceed 5% according to literature (Lepple and Brine, 1976; Lafon et
379 al., 2006; Formenti et al., 2014). The uncertainty on the estimated total clay mass, estimated between 8
380 and 26%, was calculated with the error propagation formula including the uncertainties on total dust
381 mass and on the mass of each identified mineral.

382 For the Northern African and Eastern Asian aerosols, the mass apportionment between the different
383 clay species was based on literature values of illite-to-kaolinite (I/K) and chlorite-to-kaolinite (Ch/I)



384 mass ratios (Scheuven et al., 2013; Formenti et al. 2014). For the other samples, only the total clay
 385 mass was estimated.

386

387 3. Retrieval of the LW complex refractive index

388 An optical inversion procedure was applied to retrieve the LW complex refractive index ($m=n-ik$) of
 389 the dust aerosols based on the simultaneous measurements of the particle LW spectra and size. Starting
 390 from the number size distribution, $\left[\frac{dN}{d \log D_g}\right]_{\text{CESAM}}$, the LW absorption coefficient, $\beta_{\text{abs}}(\lambda)$, meas-
 391 ured in CESAM can be calculated as:

$$392 \quad (\beta_{\text{abs}}(\lambda))_{\text{calc}} = \sum_{D_g} \frac{\pi D_g^2}{4} Q_{\text{abs}}(m, \lambda, D_g) \left[\frac{dN}{d \log D_g} \right]_{\text{CESAM}} d \log D_g \quad (5)$$

393 where $Q_{\text{abs}}(m, \lambda, D_g)$ is the particle absorption efficiency. As the simplest approach, Q_{abs} can be com-
 394 puted using Mie theory for spherical particles.

395 Our retrieval algorithm consists of iteratively varying m in expression (5) until $(\beta_{\text{abs}}(\lambda))_{\text{calc}}$ matches the
 396 measured $\beta_{\text{abs}}(\lambda)$. However, as m is a complex number with two variables, an additional condition is
 397 needed. According to electromagnetic theory, n and k must satisfy the Kramers-Kronig (K-K) relation-
 398 ship (Bohren and Huffman, 1983):

$$399 \quad n(\omega) - 1 = \frac{2}{\pi} P \int_0^{\infty} \frac{\Omega \cdot k(\Omega)}{\Omega^2 - \omega^2} \cdot d\Omega \quad (6)$$

400 with ω the angular frequency of radiation ($\omega=2\pi c/\lambda$, [s^{-1}]), and P the principal value of the Cauchy in-
 401 tegral. Equation (6) means that if $k(\lambda)$ is known, then $n(\lambda)$ can be calculated accordingly. Hence, the K-
 402 K relation is the additional condition beside (5) to retrieve n and k . A direct calculation of the K-K
 403 integral is, however, very difficult as it requires the knowledge of k over an infinite wavelength range.
 404 A useful formulation, which permits one to obtain the couple of n - k values that automatically satisfy
 405 the K-K condition, is the one based on the Lorentz dispersion theory. In the Lorentz formulation, n and
 406 k may be written as a function of the real (ϵ_r) and imaginary (ϵ_i) parts of the particle dielectric function
 407 as:

$$408 \quad n(\omega) = \left(\frac{1}{2} \left[\sqrt{(\epsilon_r(\omega))^2 + (\epsilon_i(\omega))^2} + \epsilon_r(\omega) \right] \right)^{1/2} \quad (7a)$$



$$k(\omega) = \left(\frac{1}{2} \left[\sqrt{(\epsilon_r(\omega))^2 + (\epsilon_i(\omega))^2} - \epsilon_r(\omega) \right] \right)^{1/2} \quad (7b)$$

$\epsilon_r(\omega)$ and $\epsilon_i(\omega)$ can be in turn expressed as the sum of N Lorentzian harmonic oscillators:

$$\epsilon_r(\omega) = \epsilon_\infty + \left[\sum_{j=1}^N \frac{F_j(\omega_j^2 - \omega^2)}{(\omega_j^2 - \omega^2)^2 + \gamma_j^2 \omega^2} \right] \quad (8a)$$

$$\epsilon_i(\omega) = \sum_{j=1}^N \frac{F_j \gamma_j \omega}{(\omega_j^2 - \omega^2)^2 + \gamma_j^2 \omega^2} \quad (8b)$$

where $\epsilon_\infty = n_{\text{vis}}^2$ is the real dielectric function in the limit of visible wavelengths, and n_{vis} the real part of the refractive index in the visible, and $(\omega_j, \gamma_j, F_j)$ are the three parameters (eigenfrequency, damping factor, and strength) characterizing the j -th oscillator.

In our algorithm we combined (7a)-(7) and (8a)-(8b) with (5) to retrieve n - k values that allow both to reproduce the measured $\beta_{\text{abs}}(\lambda)$ and to satisfy the K-K relationship. In practice, in the iteration procedure only one of the two components of the refractive index (in our case, k) was varied, while the other (n) was recalculated at each step based on the values of the oscillator parameters $(\omega_j, \gamma_j, F_j)$ obtained from a best fit for k . In the calculations, the initial value of $k(\lambda)$ was set at $k(\lambda) = \lambda \beta_{\text{abs}}(\lambda) / 4\pi$, then in the iteration procedure, $k(\lambda)$ was varied in steps of 0.001 without imposing any constraint on its spectral shape. Initial values of the $(\omega_j, \gamma_j, F_j)$ parameters were manually set based on the initial spectrum of $k(\lambda)$. Between 6 and 10 oscillators were needed to model the $k(\lambda)$ spectrum for the different cases. The fit between $k(\lambda)$ and Eq. (7b) was performed using the Levenberg-Marquardt technique. The iteration procedure was stopped when the condition: $|(\beta_{\text{abs}}(\lambda))_{\text{calc}} - \beta_{\text{abs}}(\lambda)| < 1\%$ is met at all wavelengths.

Optical calculations were performed between 6 and 16 μm , within a range where FTIR measured scattering could be neglected (see Sect. 2.2). Below 6 μm , $k(\lambda)$ was then fixed to the value obtained at 6 μm . Calculations were performed over 10-min intervals.

For each experiment and for each 10-min interval, the value of n_{vis} to use in Eq. (8a) was obtained from optical calculations using the simultaneous measurements of the SW scattering and absorption coefficients performed in CESAM (Di Biagio et al., in preparation). For the various aerosol samples considered here the value of n_{vis} varied between 1.47 and 1.52 with an uncertainty $< 2\%$. This approach is better than the one used in DB14, where the value of n_{vis} was manually adjusted for successive trials.



434 Specifically, in DB14, n_{vis} was varied and set to the value that allowed best reproducing the measured
435 dust scattering signal below 6 μm . As discussed in Sect. 2.2, however, only a fraction of the total dust
436 scattering is measured by the FTIR. As a result, the n_{vis} values obtained in DB14 were considerably
437 lower than the values generally assumed for dust ($n_{\text{vis}}=1.32\text{-}1.35$ compared to 1.47-1.53 from the liter-
438 ature, e.g., Osborne et al., 2008; McConnell et al., 2010), with a possible resulting overall underestima-
439 tion of n . Here, instead, the n_{vis} value was obtained based on additional SW optical measurements,
440 which ensured a more reliable estimate of the whole spectral n .

441 The validity of the proposed retrieval procedure was assessed by performing a control experiment
442 where ammonium sulfate aerosols were injected in the chamber. Ammonium sulfate has been widely
443 studied in the past and its optical properties are well known (e.g., Toon et al., 1976; Flores et al.,
444 2009). The description and the results of the control experiment are reported in Appendix 1.

445

446 **3.1 Caveats on the retrieval procedure for the LW refractive index**

447 The procedure for the retrieval of the complex refractive index presented in the previous section com-
448 bines optical calculations, the Kramers-Kronig relation and the Lorentz dispersion theory, and was
449 based on measurements of spectral absorption and particle size distribution. The approach is quite sen-
450 sitive to the accuracy and representativeness of the measurements and assumptions in the optical calcu-
451 lations. We now list the different points that need to be addressed to insure the accuracy of the retrieval
452 procedure.

453 1. First, our optical calculations (Eq. (5)) use Mie theory for spherical particles. This can introduce
454 some degrees of uncertainties in simulated LW spectra, especially near the resonant peaks (Legrand
455 et al., 2014). Since almost all climate models use Mie theory to calculate dust optical properties, we
456 decided to assume spherical particles at present. This assumption could be, however, not fully ap-
457 propriate for remote sensing applications, both ground-based and satellite, given that particle non-
458 sphericity is currently taken into account in many inversions algorithms (AERONET, POLDER,
459 etc.; e.g., Dubovik et al., 2006).

460 2. Second, as discussed in Sect. 2.2, measured dust spectra at wavelengths $> 6 \mu\text{m}$ represent only dust
461 absorption, with minimal contribution from scattering. Dufresne et al. (2002) show that the contri-
462 bution of LW scattering from dust is quite important in the atmosphere, especially under cloudy
463 conditions. Therefore, the impact of neglecting the scattering contribution has to be assessed. The



464 retrieval procedure used in this study is nearly independent of whether dust extinction or only ab-
465 sorption is used. Indeed, the combination of Eq. (5) with the Lorentz formulation in Eq. (7a) and
466 (7b) ensures the retrieval of n-k couples that are theoretically correct (fulfilling the K-K relation-
467 ship), and the specific quantity to reproduce by Eq. (5) – i.e., extinction or absorption – provides
468 only a mathematical constraint on the retrieval. Therefore, neglecting the scattering contribution to
469 the LW spectra has no influence on the estimates of the refractive index, and the real and the imagi-
470 nary parts obtained in this study represent both the scattering and the absorption components of the
471 dust extinction.

472 3. Third, optical calculations are performed only at wavelengths $> 6 \mu\text{m}$, while in the range 2-6 μm
473 $k(\lambda)$ is fixed to the value obtained at 6 μm . We examine the accuracy of this assumption. Given that,
474 over the whole 2-6 μm range, dust is expected to have a negligible absorption (k is close to zero, see
475 Di Biagio et al., 2014a), fixing k at the value at 6 μm is a reasonable approximation. Concerning the
476 impact of this assumption on the retrieval of n , it should be pointed out that in the range 2-6 μm ,
477 when k is very low, the shape of the n spectrum is determined only by the anchor point n_{vis} , and the
478 exact value of k is not relevant.

479

480 3.2 Uncertainty estimation

481 The uncertainty in the retrieved refractive index was estimated with a sensitivity analysis. Towards this
482 goal, n and k were also obtained by using as input to the retrieval algorithm the measured $\beta_{\text{abs}}(\lambda)$ and
483 size distribution \pm their estimated uncertainties. The deviations of the values of n and k retrieved in the
484 sensitivity study with respect to those obtained in the first inversion were estimated. Then, we comput-
485 ed a quadratic combination of these different factors to deduce the uncertainty in n and k .

486 The results of the sensitivity study indicated that the measurement uncertainties on $\beta_{\text{abs}}(\lambda)$ ($\pm 10\%$) and
487 the size distribution (absolute uncertainty on the number concentration, $\pm 20\text{-}70\%$) have an impact of
488 $\sim 10\text{-}20\%$ on the retrieval of n and k .

489 Additionally, a sensitivity analysis was performed to test the dependence of the retrieved LW refrac-
490 tive index on the accuracy of the shape of the size distribution above 8 μm . As discussed in Sect. 2.3.2,
491 the size distribution $\left[\frac{dN}{d\log D_g} \right]_{\text{CESAM}}$ used for the optical calculations was measured between 0.1 and
492 8 μm based on SMPS, SkyGrimm, and WELAS data. However, it was extrapolated to larger sizes by



493 applying a lognormal mode fit for particle diameters $>8 \mu\text{m}$, where measurements were not available.
494 The extrapolation was set to reproduce the shape of the WELAS size distribution between $D_g \sim 3\text{--}4$ and
495 $8 \mu\text{m}$. In the sensitivity study, n and k were also obtained by using two different size distributions as
496 input to the retrieval algorithm, in which the extrapolation curve at $D_g > 8 \mu\text{m}$ was calculated by consid-
497 ering the WELAS data \pm their estimated y -uncertainties. The results of the sensitivity study indicate
498 that a change of the extrapolation curve between its minimum and maximum may induce a variation of
499 less than 10% on the retrieved n and k .

500 The total uncertainty on n and k , estimated as the quadratic combination of these factors, was close to
501 20%.

502 An additional source of uncertainty linked to the size distribution, which however we do not quantify
503 here, concerns the choice of performing a single-mode extrapolation above $8 \mu\text{m}$, which means ne-
504 glecting the possible presence of larger dust modes.

505

506 **4. Selection of soil samples: representation of the dust mineralogical variability at the global** 507 **scale**

508 Nineteen soil samples were selected for experiments from a collection of 137 soils from various source
509 areas worldwide. Their location is shown in Fig. 2. The main information on the provenance of the
510 selected soils is summarized in Table 2. Soils were grouped in the nine regions identified by Ginoux et
511 al. (2012): Northern Africa, Sahel, Eastern Africa and Middle East, Central Asia, Eastern Asia, North
512 America, South America, Southern Africa, and Australia. The choice of the soils to analyze was per-
513 formed according to two criteria: 1) soils had to represent all major arid and semi-arid regions, as de-
514 picted by Ginoux et al. (2012) and 2) their mineralogy should envelope the largest possible variability
515 of the soil mineralogical composition at the global scale.

516 A large set of soils were available for Northern Africa, the Sahel, Eastern Africa and the Middle East,
517 Eastern Asia, and Southern Africa. Here, the selection was performed using as guidance the global
518 database of Journet et al. (2014), reporting the composition of the clay ($<2 \mu\text{m}$ diameter) and silt (<60
519 μm diameter) fractions in terms of 12 different minerals. Amongst them, we analyzed the variability of
520 the minerals that are most abundant in dust as well as most optically relevant to LW absorption, name-
521 ly, illite, kaolinite, calcite, and quartz in the clay fraction, and calcite and quartz in the silt fraction. The



522 comparison of the extracted (from the Journet database) clay and silt compositions of the soils corre-
523 sponding to the available samples resulted in the selection of five samples for Northern Sahara, three
524 for the Sahel, three for Eastern Africa and the Middle East, and two for Eastern Asia and Southern
525 Africa, as listed in Table 2.

526 For Northern Africa, we selected soils from the Northern Sahara (Tunisia, Morocco), richer in calcite
527 and illite, Central Sahara (Libya and Algeria), enriched in kaolinite compared to illite and poor in cal-
528 cite, and Western Sahara (Mauritania), richer in kaolinite. The three samples from the Sahel are from
529 Niger, Mali and Chad (sediment from the Bodélé depression), and are enriched in quartz compared to
530 Saharan samples. The selected soils from Northern Africa and the Sahel represent important sources
531 for medium and long-range dust transport towards the Mediterranean (Israelevich et al., 2002) and the
532 Atlantic Ocean (Prospero et al., 2002; Reid et al., 2003). In particular, the Bodélé depression is one of
533 the most active sources at the global scale (Goudie and Middleton, 2001; Washington et al., 2003).

534 The three soils from Eastern Africa and the Middle East are from Ethiopia, Saudi Arabia, and Kuwait,
535 which are important sources of dust in the Red and the Arabian seas (Prospero et al., 2002) and the
536 North Indian Ocean (Leon and Legrand, 2003). These three samples differ in their content of calcite,
537 quartz, and illite-to-kaolinite mass ratio (I/K).

538 For the second largest global source of dust, Eastern Asia, we considered two samples representative
539 of the Gobi and the Taklimakan deserts, respectively. These soils differ in their content of calcite and
540 quartz. Unfortunately, no soils are available for Central Asia, mostly due to the difficulty of sampling
541 these remote desert areas.

542 For Southern Africa, we selected two soils from the Namib desert, one soil from the area between the
543 Kuiseb and Ugab valleys (Namib-1) and one soil from the Damaraland rocky area (Namib-2), both
544 sources of dust transported towards the South-Eastern Atlantic (Vickery et al. 2013). These two soils
545 present different compositions in term of calcite content and I/K ratio.

546 A very limited number of samples were available in the soil collection for North and South America
547 and Australia. These soils were collected in the Sonoran Desert for North America, in the Atacama and
548 Patagonian deserts for South America, and in the Strzelecki desert for Australia. The Sonoran Desert is
549 a permanent source of dust in North America, the Atacama desert is the most important source of dust
550 in South America, whilst Patagonia emissions are relevant for long-range transport towards Antarctica



551 (Ginoux et al., 2012). The Strzelecki desert is the seventh largest desert of Australia. No mineralogical
552 criteria were applied to these areas.

553 A summary of the mineralogical composition of the nineteen selected soils is shown in Fig. 3 in com-
554 parison with the full range of variability obtained considering the full data from the different nine dust
555 source areas. As illustrated by this figure, the samples chosen for this study cover the entire global
556 variability of the soil compositions derived by Journet et al. (2014).

557

558 **5. Results**

559 **5.1 Atmospheric representativity: mineralogical composition**

560 The mineralogical composition of the nineteen generated aerosol samples as measured by XRD analy-
561 sis is shown in Fig. 4. The aerosol composition is dominated by clays (~55-95% for the different sam-
562 ples), with variable contents of quartz, calcite, dolomite, and feldspars. Identified clay species are: il-
563 lite, kaolinite, smectite, palygorskite, and chlorite. Illite and kaolinite are ubiquitous; smectite and
564 palygorskite are detected in some of the samples (Algeria, Ethiopia, Saudi Arabia, Kuwait, Arizona,
565 and both samples from Namibia); in contrast, chlorite is found only in the two Chinese and in the Chil-
566 ean samples. The estimated contribution of illite, kaolinite and chlorite to the total clay mass are shown
567 in Fig. 4 for Northern Africa (Algerian sample excluded, given that also smectite is detected in this
568 sample) and Eastern Asian aerosols. Quartz ranges from 2 to 32% by mass in the samples, with the
569 highest values measured for Australia, Patagonia, and Niger dust. Calcite is less than 17%, with maxi-
570 ma observed for Tunisia and Gobi dusts. Conversely, minor traces of dolomite (<2%) are detected in
571 all the different samples. Finally, feldspars (orthoclase and albite) represent less than 9% of the dust
572 composition.

573 Observations from the present study capture well the global tendencies of the dust mineralogical com-
574 positions as observed in several studies based on aerosol field observations, both from ground-based
575 and airborne samples (e.g., Sokolik and Toon, 1999; Caquineau et al., 2002; Shen et al., 2005; Jeong,
576 2008; Kandler et al., 2009; Scheuvens et al., 2013; Formenti et al., 2014). For instance, at the scale of
577 Northern Africa, we correctly reproduce the geographical distribution of calcite, which is expected to
578 be larger in Northern Saharan samples (Tunisia, Morocco), and very low or absent when moving to-
579 wards the Southern part of the Sahara and the Sahel (Libya, Algeria, Mauritania, Niger, Mali, and Bo-



580 délé samples). Similarly, we observe an increase of the aerosol quartz content from Northern Sahara
 581 towards the Sahel, which is well known at the regional scale of Northern Africa (e.g., Caquineau et al.,
 582 2002). Also, we identify the presence of chlorite in the Eastern Asian samples (Gobi and Taklimakan),
 583 in agreement with field observations in this region (Shen et al., 2005). A more direct comparison of
 584 our data with field measurements of the dust mineralogical composition is rather complicated due to
 585 possible differences linked to the size distribution and representativeness of the specific sources be-
 586 tween our data and field measurements (Perlwitz et al., 2015a, 2015b). For the Niger sample only,
 587 however, a semi-quantitative comparison can be performed against field data of the dust mineralogy
 588 obtained for aerosols collected at Banizoumbou during the AMMA (African Monsoon Multidiscipli-
 589 nary Analysis) campaign in 2006. The mineralogy for these samples was provided by Formenti et al.
 590 (2014). For a case of intense local erosion at Banizoumbou, they showed that the aerosol is composed
 591 of 51% (by volume) of clays, 41% of quartz, and 3% of feldspars. Our Niger sample generated from
 592 the soil collected at Banizoumbou, is composed of 64% of clays, 30% of quartz, and 5% of feldspars,
 593 in relatively good agreement with the field observations.

594

595 **5.2 Atmospheric representativity: size distribution**

596 The size distribution of the dust aerosols measured at the peak of the dust injection in the chamber is
 597 shown in Fig. 5. We report in the plot the normalized surface size distribution, defined as:

$$598 \quad \frac{dS}{d \log D_g} (\text{normalized}) = \frac{1}{S_{\text{tot}}} \cdot \left(\frac{\pi}{4} D_g^2 \left[\frac{dN}{d \log D_g} \right]_{\text{CESAM}} \right) \quad (9)$$

599 with S_{tot} the total surface area. The surface size distribution is the quantity that determines dust optical
 600 properties (see Eq. 5). The dust surface size distributions present multimodal structures, where the
 601 relative proportions of the different modes vary significantly between the samples. The dust mass con-
 602 centration at the peak of the injection estimated from size distribution data varies between 2 and 310
 603 mg m^{-3} . These values are comparable to what has been observed close to sources in proximity to dust
 604 storms (Goudie and Middleton, 2006; Rajot et al., 2008; Kandler et al., 2009; Marticorena et al., 2010).
 605 Given that the protocol used for soil preparation and aerosol generation is always the same for the dif-
 606 ferent experiments, the observed differences in both the shape of the size distribution and the mass
 607 concentration of the generated dust aerosols are attributed to the specific characteristics of the soils,
 608 which may be more or less prone to produce coarse-size particles.



609 The comparison of the chamber data with observations of the dust size distribution from several air-
610 borne campaigns in Africa and Asia is shown in Fig. 6. This comparison suggests that the shape of the
611 size distribution in the chamber at the peak of the injection accurately mimic the dust distribution in
612 the atmosphere near sources.

613 The time evolution of the normalized surface size distribution within CESAM is shown in Fig. 7 for
614 two examples taken from the Algeria and Atacama experiments, while an example of the dust number
615 and mass concentration evolution over an entire experiment is illustrated in Fig. S5 (supplementary
616 material). As shown in Fig. 7, the dust size distribution strongly changes with time due to gravitational
617 settling: the coarse mode above 5 μm rapidly decreases, due to the larger fall speed at these sizes (~ 1
618 cm s^{-1} at 10 μm , compared to $\sim 0.01 \text{ cm s}^{-1}$ at 1 μm ; Seinfeld and Pandis, 2006), and the relative im-
619 portance of the fraction smaller than $D_g=5 \mu\text{m}$ increases concurrently. In the chamber we are thus able
620 to reproduce very rapidly (about 2 hours) the size-selective gravitational settling, a process that in the
621 atmosphere may takes about one to five days to occur (Maring et al., 2003). In order to compare the
622 dust gravitational settling in the chamber with that observed in the atmosphere the following analysis
623 was performed. For both Algeria and Atacama soils, the fraction of particles remaining in suspension
624 in the chamber as a function of time versus particle size was calculated as $dN_i(D_g)/dN_0(D_g)$, where
625 $dN_i(D_g)$ is the number of particles measured by size class at the i -time (i corresponding to 30, 60, 90
626 and 120 min after injection) and $dN_0(D_g)$ represents the size-dependent particle number at the peak of
627 the injection. The results of these calculations are shown in the lower panels of Fig. 7, where they are
628 compared to the fraction remaining airborne after 1-2 days obtained in the field study by Ryder et al.
629 (2013b) for mineral dust transported out of Northern Africa in the Saharan Air Layer (Karyampudi et
630 al., 1999), that is, at altitudes between 1.5 and 6 km above sea level. The comparison indicates that the
631 remaining particle fraction observed 30 minutes after the peak of the injection is comparable to that
632 obtained by Ryder et al. (2013b) for particles smaller than ~ 3 to 8 μm (depending on the soil) but that
633 the depletion is much faster for larger particles. This suggests, on the one hand, that the number frac-
634 tion of coarse particles in the chamber depends on the initial size distribution, that is, on the nature of
635 the soil itself. On the other hand, it shows the limitation of the four-blade fan in providing a vertical
636 updraft sufficient to counterbalance the gravimetric deposition for particles larger than about 8 μm .
637 This point, however, is not surprising since it is clear that in the laboratory it is not possible to repro-
638 duce the wide range of dynamical processes that occur in the real atmosphere, and so to obtain a faith-
639 ful reproduction of dust gravitational settling and the counteracting re-suspension mechanisms. None-



640 theless, it should be noted that the rate of removal is higher at the earlier stage of the experiments than
641 towards their end. The size-dependent particle lifetime, defined as the value at which dN/dN_0 is equal
642 to $1/e$ (McMurry and Rader, 1985), is relatively invariant for particles smaller than $D_g < \sim 2 \mu\text{m}$ (> 60
643 min). This indicates that no significant distortion of the particle size distribution occurs after the most
644 significant removal at the beginning of the experiment, and that the fine-to-coarse proportions are
645 modified with time in a manner consistent with previous field observations on medium- to long-
646 transport (e.g., Maring et al., 2003; Rajot et al., 2008; Reid et al., 2008; Ryder et al., 2013b; Denjean et
647 al., 2016).

648

649 **5.3 Dust LW extinction and complex refractive index spectra for the different source regions**

650 Figure 8 shows the dust LW spectral extinction coefficients measured at the peak of the injection for
651 the nineteen aerosol samples. As discussed in Sect. 2.2, the spectra in Fig. 8 show the contribution of
652 dust scattering below $6 \mu\text{m}$, while the absorption spectrum only is measured above $6 \mu\text{m}$. In this wave-
653 length range, significant differences are observed when comparing the samples, which in turn are
654 linked to differences in their mineralogical composition.

655 Figure 8 allows the identification of the spectral features of the minerals presenting the strongest ab-
656 sorption bands, in particular in the $8\text{--}12 \mu\text{m}$ atmospheric window (Table 3). The most prominent ab-
657 sorption peak is found around $9.6 \mu\text{m}$ for all samples, where clays have their Si—O stretch resonance
658 peak. The shape around the peak differs according to the relative proportions of illite and kaolinite in
659 the samples, as is illustrated with the results for Tunisia, Morocco, Ethiopia, Kuwait, Arizona, Patago-
660 nia, Gobi and Taklimakan samples (richer in illite) compared to Libya, Algeria, Mauritania, Niger,
661 Bodélé, Saudi Arabia, and Australia (richer in kaolinite). Aerosols rich in kaolinite also show a sec-
662 ondary peak at $\sim 10.9 \mu\text{m}$. The spectral signature of quartz at 9.2 and $12.5\text{--}12.9 \mu\text{m}$ is ubiquitous, with
663 a stronger contribution in the Bodélé, Niger, Patagonia, and Australia samples. Aerosols rich in calcite,
664 such as the Tunisia, Morocco, Saudi Arabia, Taklimakan, Arizona, Atacama, and Namib-1 samples
665 show absorption bands at ~ 7 and $11.4 \mu\text{m}$. Conversely, these are not present in the other samples and
666 in particular in none of the samples from the Sahel. Finally, the contribution of feldspars (albite) at 8.7
667 μm is clearly detected only for the Namib-1 sample.

668 The intensity of the absorption bands depend strongly on the particle size distribution, in particular on
669 the contribution of the aerosol super-micron fraction, as well as on the total dust mass concentration.



670 These, as discussed in the previous section, are associated with the specific characteristics of each of
671 the soils used and their propensity for dust emission. The highest values of dust absorption that can be
672 seen in Fig. 8 for the 8–12 μm spectral region appear for the Bodélé aerosol sample. In this particular
673 sample, the super-micron particles represent 45% of the total particle number at the peak of the injec-
674 tion, and this sample showed the highest mass concentration in the chamber (310 mg m^{-3}). Conversely,
675 the lowest absorption is measured for the aerosols from Mauritania, Mali, Kuwait, and Gobi, for which
676 the super-micron particle fraction and the mass concentrations are lower.

677 The intensity of the spectral extinction rapidly decreases after injection, following the decrease of the
678 super-micron particle number and mass concentration. As an example, Fig. 9 shows the temporal evo-
679 lution of the measured extinction spectrum for the Algeria and Atacama aerosols. The intensity of the
680 absorption band at $9.6 \mu\text{m}$ is about halved after 30 min and reduced to $\sim 20\text{--}30\%$ and $<10\%$ of its initial
681 value after 60 min and 90–120 min, respectively. Because of the size-dependence of the mineralogical
682 composition, notably the relative proportions of quartz and calcite with respect to clays (Pye et al.,
683 1987), settling could also modify the spectral shape of the extinction spectrum. This effect was inves-
684 tigated for the two example cases, Algeria and Atacama, by looking at the temporal evolution of the
685 ratios of the measured extinction coefficient in some specific mineral absorption bands. Changes
686 would indicate that the time variability of the mineralogical composition is optically significant. For
687 the Algeria case, we have considered the quartz ($12.5 \mu\text{m}$) versus clay ($9.6 \mu\text{m}$) bands, and for the
688 Atacama case the calcite ($\sim 7 \mu\text{m}$) versus clay ($9.6 \mu\text{m}$) bands. For both cases, the calculated ratios do
689 not change significantly with time, i.e. they agree within error bars: for Algeria, the quartz-to-clay ratio
690 is 0.21 ± 0.03 at the peak of the injection and 0.25 ± 0.04 120 min later; for Atacama, the calcite-to-clay
691 ratio is 0.73 ± 0.10 and 0.67 ± 0.09 for the same times. Similar results were also obtained for the other
692 samples, with the only exception of Saudi Arabia and Morocco for which we observed an increase of
693 the calcite-to-clay ratio with time. The time invariance of the quartz-to-clays and calcite-to-clays ratios
694 observed for the majority of the analyzed aerosol samples agrees with the observations of the size-
695 dependent dust mineralogical composition obtained by Kandler et al. (2009). These authors showed
696 that in the super-micron diameter range up to $\sim 25 \mu\text{m}$, i.e. in the range where dust is mostly LW-
697 active, the quartz/clay and calcite/clay ratios are approximately constant with size. This would suggest
698 that the loss of particles in this size range should not modify the relative proportions of these minerals,
699 and thus their contributions to LW absorption. Nonetheless, the different behavior observed for Saudi



700 Arabia and Morocco would possibly indicate differences in the size-dependence of the mineralogical
701 composition compared to the other samples.

702 For each soil, the estimated real (n) and imaginary (k) parts of the complex refractive index are shown
703 in Fig. 10. The reported n and k correspond to the mean of the 10-min values estimated between the
704 peak of the injection and 120 min later. This can be done because, for each soil, the time variation of
705 the complex refractive index is moderate. Standard deviations, not shown in Fig. 10 for the sake of
706 visual clarity, are <10% for n and <20% for k. Figure 10 shows that the dust refractive index widely
707 varies both in magnitude and spectral shape from sample to sample, following the variability of the
708 measured extinction spectra. The real part n varies between 0.84 and 1.94, while the imaginary part k
709 is between ~0.001 and 0.92.

710

711 **6. Discussion**

712 **6.1 Predicting the dust complex refractive index based on its mineralogical composition**

713 Our results show that the LW refractive index of mineral dust having different mineralogical composi-
714 tions varies considerably. Nevertheless, at wavelengths where the absorption peaks due to different
715 minerals do not overlap, this variability can be predicted from the composition-resolved mass concen-
716 trations. These considerations are illustrated in Fig. 11, where we relate the mean values of the dust k
717 in the calcite, quartz, and clay absorption bands between 7.0 and 11.4 μm to the percent mass fraction
718 of these minerals in the dust. Mean k values were calculated as averages over the filter sampling times.
719 For calcite and quartz (resonance peaks at 7.0, 9.2, and 11.4 μm), this relation is almost linear. These
720 two minerals are commonly large in grain size and well crystallized. Their quantification by XRD is
721 certain and they produce a strong and well-identified absorption peak in the LW. Nonetheless, there
722 seems to be a lower limit of the percent mass of calcite (around 5%) that gives rise to absorption at 7
723 μm , and therefore measurable k-values (Fig. 11). Conversely, at 11.4 μm , non-zero k-values are ob-
724 tained even in the absence of calcite, due to the interference of the calcite peak and the clay resonance
725 bands.

726 Poorer or no correlation is found between k and the percent mass fraction in the absorption bands of
727 clays at 9.6 and 10.9 μm . This different behavior is not unexpected. Clay minerals such as kaolinite,
728 illite, smectite and chlorite are soil weathering products containing aluminium and silicon in a 1:1 or



729 1:2 ratio (tetrahedral or octahedral structure, respectively). As a consequence, the position of their vi-
730 brational peaks is very similar (Dorschner et al., 1978; Querry, 1987, Glotch et al., 2007). In the at-
731 mosphere, these minerals undergo aging by gas and water vapor adsorption (Usher et al., 2003; Schut-
732 tlefield et al., 2007). As a result of the production conditions in the soils (weathering) and aging in the
733 atmosphere, their physical and chemical conditions (composition, crystallinity, aggregation state)
734 might differ from one soil to the other, and from that of mineralogical standards. That is the reason
735 why XRD measurements of clays in natural dust samples might be erroneous, and why we prefer to
736 estimate the clay fraction indirectly. Nonetheless, the indirect estimate is also prone to error, and de-
737 pends strongly on an independent estimate of the total mass (which, in the presence of large particles
738 can be problematic) as well as the correct quantification of the non-clay fraction. This is likely reflect-
739 ed in the large scatter observed in Fig. 11 when trying to relate the k-value distribution to the corre-
740 sponding percent mass of clays. These considerations also affect the speciation of clays, and explain
741 the similar results obtained when separately plotting the spectral k-values against the estimate kaolinite
742 or illite masses. The superposition of the resonance bands of these two clays, as well as those of the
743 smectites, which in addition are often poorly crystallized and therefore difficult to detect by XRD, as
744 well as those in the quartz absorption band at 9.2 μm , suggests that a more formal spectral deconvolu-
745 tion procedure based on single mineral reference spectra is needed to understand the shape and magni-
746 tude of the refractive index in this spectral band.

747

748 **6.2 Dust complex refractive index versus size distribution during atmospheric transport**

749 Quantifying the radiative impact of dust depends not only on the ability to provide spatially-resolved
750 optical properties, but also on the accurate representation of the possible changes of these properties
751 during transport. In the LW, this effect is amplified by the changes in the size distribution, particularly
752 the loss of coarse particles. Our experiments accurately capture the overall features of the dust size
753 distribution, including the extent and modal position of the coarse particle mode. However, the deple-
754 tion rate with time for coarse particles is higher than observed in the atmosphere (e.g., Ryder et al.,
755 2013b). The size distribution after 30 minutes still contains a significant, relatively invariant, but not-
756 predictable fraction of coarse particles. This calls for two considerations: 1) the refractive indices ob-
757 tained at the early stage of the experiments (within 30 minutes after the dust injection) are representa-
758 tive of dust at short to medium ranges of transport; 2) the refractive indices after 30 minutes of dura-



759 tion are likely to represent long-range transported dust still containing coarse particles in a fraction that
760 will depend on the original soil. In our study, the calculated refractive indices do not change with time
761 in parallel with the observed changes in the size distribution, thus suggesting that a constant value can
762 be assumed close to the source and during transport. Still, further experiments taking into account only
763 the fine fraction of the aerosols will be needed to constrain the size-dependence of the refractive index.

764

765 **6.3 Comparison with the literature**

766 In Fig. 12, we compare our results with estimates of the dust refractive index reported in the literature.
767 We consider data by Volz (1972, 1973) for dust collected in Germany and at Barbados, Fouquart et al.
768 (1987) for Niger sand, and Di Biagio et al. (2014a) for dust from Algeria and Niger. We also report
769 data for dust as assumed in the OPAC database (Optical Properties of Aerosols and Clouds; Hess et al.,
770 1998; Koepke et al., 2015), one of the most frequently used references in climate modeling and remote
771 sensing applications. Because of the limited regional span, the literature data clearly cannot do justice
772 to the full range of magnitude and of the spectral variability of the LW complex refractive index that is
773 presented in our dataset. In particular, clearly none of the published data represent the contribution of
774 calcite at $\sim 7 \mu\text{m}$. Some of the data (Volz, 1973; Fouquart et al., 1987; OPAC) overestimate k above 11
775 μm , where the 12.5-12.9 μm quartz absorption band is found. The best correspondence, especially
776 above 10 μm , is found with Di Biagio et al. (2014a). In the 8–12 μm atmospheric window, the agree-
777 ment with our estimated mean value is moderate, but the range of variability around the mean and its
778 spectral dependence are underrepresented. A shift towards larger wavelengths is also observed for the
779 main clay absorption peak at $\sim 9.6 \mu\text{m}$ for Volz (1973) and Di Biagio et al. (2014a), which is possibly
780 linked to the different method used in these studies to retrieve the complex refractive index (pellet
781 spectroscopy approach) compared to our data. The agreement is even less satisfactory for the real part
782 of the refractive index (upper panel of Fig. 12), which is overestimated in OPAC and Volz (1973) and
783 underestimated in Fouquart et al. (1987). As discussed in Di Biagio et al. (2014a), differences for the
784 real part between the various studies come mostly from the different methods used to estimate the dust
785 refractive index. The methods used in the literature most often do not fulfil the Kramers-Kronig rela-
786 tionship for the n - k couples. The only dataset that fulfils the Kramers-Kronig relationship is Fouquart
787 et al. (1987), but that has the drawback of underestimating n as a consequence of the low value of n_{vis}
788 (~ 1) assumed in the retrieval.



789 7. Conclusions and perspectives

790 In this study we have presented a new set of laboratory in situ measurements of the LW extinction
791 spectra and complex refractive indices of mineral dust aerosols from nineteen natural soils from source
792 regions in Northern Africa, Sahel, Middle East, Eastern Asia, North and South America, Southern Af-
793 rica, and Australia. These sources are representative of the heterogeneity of the dust composition at the
794 global scale. Consequently, the envelope of refractive index data obtained in this study can adequately
795 represent the full range of variability for dust as function of the global variability of its mineralogical
796 composition. These data are expected to be widely applicable for both radiative transfer modelling and
797 remote sensing applications.

798 The experiments described here were conducted in the realistic and dynamic environment of the 4.2 m³
799 CESAM chamber. Dust aerosols generated in the chamber are characterized by a realistic size distribu-
800 tion, including both the sub-micron and the super-micron fraction, and they have an atmospherically
801 representative mineralogical composition, including the main LW active minerals, such as quartz,
802 clays, and calcite. The complex refractive index of dust at LW wavelengths is obtained following a
803 rigorous approach that permits to determine n-k couples that satisfy the Kramers-Kronig relation. Re-
804 fractive index data from the present study are much more reliable than those provided by DB14, given
805 that a better estimate of n_{vis} was used in the retrieval algorithm. The average uncertainty in the ob-
806 tained n and k is ~20%.

807 The main results from this work can be summarized as follows.

- 808 1. The LW refractive index of dust varies strongly both in magnitude and spectral shape as a result of
809 the variability of the particle mineralogy related to the source region of emission. The available lit-
810 erature data (Volz, 1972, 1973; Fouquart et al., 1987; OPAC, Hess et al., 1998, Koepke et al., 2015)
811 used nowadays in climate models and satellite retrievals, do not adequately represent either the
812 magnitude, or the spectral features and the variability of the LW refractive index of mineral dust
813 observed in our dataset. In consequence, we recommend the use of source-specific extinction spec-
814 tra/refractive indices rather than generic values.
- 815 2. We observe a linear relationship between the magnitude of the LW refractive index and the mass
816 concentration of specific minerals, i.e., quartz and calcite. This opens the possibility of providing
817 predictive relationships to estimate the LW refractive index of dust at specific bands based on an as-
818 sumed or predicted mineralogical composition, or conversely, to estimate the dust composition



819 (even partially) from measurements of LW extinction at specific wavebands. This could have im-
820 portant implications for the representation of LW optical properties of dust in climate models,
821 which have started to incorporate the representation of dust mineralogy in their schemes (Scanza et
822 al., 2015; Perlwitz et al., 2015a). In addition, the possibility to relate the mass of minerals to the ab-
823 sorption at specific bands implies that the LW extinction spectra measured from space-can be used
824 to distinguish between different dust sources.

825 3. The spectral shape of the dust extinction spectrum does not seem to change significantly with time
826 due to the loss of coarse particles by gravitational settling. This suggests that, despite the dust
827 coarse mode being increasingly depleted, the relative proportions of minerals do not change signifi-
828 cantly with time or at least that their changes do not affect the overall optical response of the dust
829 samples. In consequence, the retrieved LW refractive index does not change, and therefore can be
830 used to represent short-to-medium range transport conditions. This finding supports the common
831 practice in global models to treat the dust LW refractive index as static during transport. This also
832 implies that to represent the dust LW refractive index vs mineralogy, models just have to reproduce
833 the dust composition at the source, without the necessity of following its changes during transport,
834 which could be a challenge. This would considerably simplify the representation of dust mineralogy
835 in models.

836 The unique dataset presented in this study should be particularly useful for improving the dust-climate
837 interactions within regional and global models, and to take into account the geographical variability of
838 the dust LW refractive index, which at present is not represented. This will allow obtaining a more
839 realistic representation of the dust LW effect and its radiative forcing upon climate. To date, as evi-
840 denced in Boucher et al. (2013), the sign of the dust direct effect remains unknown. In this regard, in
841 particular, we estimate lower dust absorption than in OPAC (see k curves in Fig. 12). The integral of
842 the OPAC dust refractive index (imaginary part) between 3 and 15 μm is about 20% larger compared
843 to the integral obtained from our max k curve; up to about one order of magnitude overestimate is
844 found when the integral of the OPAC k over the 3-15 μm range is compared to the integral of our min
845 k curve. In consequence of this, we can conclude that the use of OPAC data may introduce a systemat-
846 ic bias in modelling dust radiative effects at LW wavelengths.



847 The use of data from the present study also will help reducing uncertainties in satellite retrievals, thus
848 contributing to improve the remote sensing capability over regions affected by dust (e.g., Capelle et al.,
849 2014; Cuesta et al., 2015).

850 The work presented in this paper also opens various perspectives.

851 First, the results of the present study clearly suggest that the LW refractive index of dust varies at the
852 regional scale, as can be observed in Fig. 10 for Northern Africa, Sahel, the Middle East, Eastern Asia,
853 South America and Southern Africa. This regional variability has to be characterized further in order to
854 better assess the influence of dust on regional climate.

855 Second, the possibility of a more formal spectral deconvolution procedure based on single mineral
856 reference spectra to understand the shape, magnitude, and temporal variability of the refractive index
857 in all different spectral bands must be investigated. This could strongly help finding robust relation-
858 ships linking the dust refractive index to the particle mineralogy.

859 Third, further experimental efforts by increasing the lifetime and selecting size classes will be needed
860 to verify better the applicability of the obtained refractive index to long-range transport conditions.
861 Also, the experiments described here were done in conditions when dry deposition is the only aging
862 process. Other aging processes, such as heterogeneous reactions, mixing with other aerosol types, or
863 water uptake, have to be investigated to evaluate their impact on the LW refractive index during
864 transport. For instance, some studies suggest a possible enhancement of dust LW absorption over spe-
865 cific bands if water uptake occurs (Schuttlefield et al., 2007) or if dust mixes with soot (Hansell et al.,
866 2011).

867

868 **Appendix 1. Control experiment with ammonium sulfate particles**

869 In order to validate the methodology applied in this study, a control experiment was performed on
870 ammonium sulfate aerosols. Particles were generated from a 0.03 M solution of ammonium sulfate
871 using a constant output atomizer (TSI, model 3075). The aerosol flow passed through a diffusion drier
872 (TSI, model 3062), to be then injected in the CESAM chamber at a flow of 10 L min⁻¹ for 10 minutes.
873 At the peak of the injection the aerosol concentration reached ~160 µg m⁻³ and the size distribution
874 was mono-modal and centered at ~0.06 µm. The LW spectrum of ammonium sulfate measured in
875 CESAM at the peak of the injection is shown in Fig. A1 for the 2-15 µm range. Absorption bands at-
876 tributed to gas-phase water vapor and CO₂ present in the chamber during the experiments are indicated



877 in the plot. The 2-15 μm spectral region includes three of the four active vibrational modes of the am-
878 monium sulfate salt: $\nu_3(\text{NH}_4^+)$ (3230 cm^{-1} or $3.10\ \mu\text{m}$), $\nu_4(\text{NH}_4^+)$ (1425 cm^{-1} or $7.02\ \mu\text{m}$; not identified
879 in the plot due to its superposition with the water vapor band), and $\nu_3(\text{SO}_2^{-4})$ (1117 cm^{-1} or $8.95\ \mu\text{m}$).
880 The $\nu_4(\text{SO}_2^{-4})$ is at 620 cm^{-1} ($16.12\ \mu\text{m}$), thus below the measurement range of the FTIR. The retrieval
881 algorithm described in Sect. 3 was applied to estimate the complex refractive index of ammonium sul-
882 fate aerosols. Calculations were performed only in the 8-10 μm range where the $\nu_3(\text{SO}_2^{-4})$ band is
883 found and where the contamination by water vapor is minimal. The value of n_{vis} to use as input to the
884 algorithm was set at 1.55, based on the analysis of simultaneous SW optical data (not discussed here).
885 The results of the calculations are shown in Fig. A1. The comparison with the optical constants pro-
886 vided by Toon et al. (1976), also shown in Fig. A1, is very satisfactory. A small bias is observed for
887 our retrieved n compared to the values by Toon et al. (1976). This can be possibly linked to the method
888 used in Toon et al. (1976) to retrieve the real part of the refractive index, which is based on the meas-
889 urement of the normal incident reflectivity of a bulk sample instead of absorption data of aerosol parti-
890 cles, as in our experiments. Overall, the results of the control experiment indicate that the CESAM
891 approach and the proposed retrieval algorithm allow to reproduce the LW spectral signature of the
892 aerosols and to estimate accurately their complex refractive index.

893

894

895

896

897

898

899

900

901

902

903

904



905 **Author contributions**

906 C. Di Biagio, P. Formenti, Y. Balkanski, and J. F. Doussin designed the experiments and discussed the
907 results. C. Di Biagio realized the experiments and performed the full data analysis with contributions
908 by P. Formenti, L. Caponi, M. Cazaunau, E. Pangui, S. Caquineau, and J.F. Doussin. S. Nowak per-
909 formed the XRD measurements. M. O. Andreae, K. Kandler, T. Saeed, S. Piketh, D. Seibert, and E.
910 Williams collected the soil samples used for experiments. E. Journet participated to the selection of the
911 soil samples for experiments and contributed to the scientific discussion. C. Di Biagio, P. Formenti,
912 and Y. Balkanski wrote the manuscript with comments from all co-authors.

913

914 **Acknowledgements**

915 This work was supported by the French national programme LEFE/INSU, by the EC within the I3 pro-
916 ject “Integration of European Simulation Chambers for Investigating Atmospheric Processes” (EU-
917 ROCHAMP-2, contract no. 228335), by the OSU-EFLUVE (Observatoire des Sciences de l’Univers-
918 Enveloppes Fluides de la Ville à l’Exobiologie) through dedicated research funding, and by the CNRS-
919 INSU supporting CESAM as national facility. C. Di Biagio was supported by the CNRS via the Labex
920 L-IPSL. K. Kandler received support from the German Science Foundation DFG (KA 2280/2). Field
921 sampling in Saudi Arabia was supported by a grant from King Saud University. The authors strongly
922 thank S. Alfaro, B. Chatenet, M. Kardous, R. Losno, B. Marticorena, J. L. Rajot, and G. Vargas, who
923 participated in the collection of the soil samples from Tunisia, Niger, Atacama, Patagonia, and the Go-
924 bi desert used in this study. The authors wish also to acknowledge J.L Rajot for his helpful comments.

925

926

927

928

929

930

931

932

933

934

935 **References**

- 936 Alfaro, S. C., Lafon, S., Rajot, J. L., Formenti, P., Gaudichet, A., and Maillé, M.: Iron oxides and light
937 absorption by pure desert dust: an experimental study, *J. Geophys. Res.*, 109, D08208,
938 doi:10.1029/2003JD004374, 2004.
- 939 Balkanski, Y., Schulz, M., Claquin, T., and Guibert, S.: Reevaluation of mineral aerosol radiative forc-
940 ings suggests a better agreement with satellite and AERONET data, *Atmos. Chem. Phys.*, 7, 81–95,
941 doi:10.5194/acp-7-81-2007, 2007.
- 942 Bohren, C. E. and Huffman, D. R.: *Absorption and Scattering of Light by Small Particles*, Wiley, New
943 York, 1983.
- 944 Boucher, O., et al., *Clouds and Aerosols*. Stocker, T., & Qin, D. (eds), *Climate Change 2013: The*
945 *Physical Science Basis. Contribution of Working Group I to the Fifth Assessment Report of the In-*
946 *tergovernmental Panel on Climate Change*. Cambridge Univ. Press, Cambridge, United Kingdom
947 and New York, NY, USA, 2013.
- 948 Capelle, V., Chédin, A., Siméon, M., Tsamalis, C., Pierangelo, C., Pondrom, M., Crevoisier, C., Cre-
949 peau, L., and Scott, N. A.: Evaluation of IASI-derived dust aerosol characteristics over the tropical
950 belt, *Atmos. Chem. Phys.*, 14, 9343–9362, doi:10.5194/acp-14-9343-2014, 2014.
- 951 Caquineau, S., Magonthier, M. C., Gaudichet, A., and Gomes, L.: An improved procedure for the X-
952 ray diffraction analysis of low-mass atmospheric dust samples, *Eur. J. Mineral.*, 9, 157–166, 1997.
- 953 Caquineau, S., Gaudichet, A., Gomes, L., and Legrand, M.: Mineralogy of Saharan dust transported
954 over northwestern tropical Atlantic Ocean in relation to source regions, *J. Geophys. Res.*,
955 107(D15), 4251, doi:10.1029/2000JD000247, 2002.
- 956 Claquin, T., Schulz, M., Balkanski, Y. J., and Boucher, O.: Uncertainties in assessing radiative forcing
957 by mineral dust, *TellusB*, 50, 491–505, 1998.
- 958 Claquin, T., Schulz, M., and Balkanski, Y. J.: Modeling the mineralogy of atmospheric dust sources, *J.*
959 *Geophys. Res.*, 104, 22243–22256, 1999.
- 960 Clarke, A. D., Shinozuka, Y. V., Kapustin, N., Howell, S., Huebert, B., Doherty, S., Anderson, T.,
961 Covert, D., Anderson, J., Hua, X., Moore II, K. G., McNaughton, C., Carmichael, G., and Weber,
962 R.: Size distributions and mixtures of dust and black carbon aerosol in Asian outflow: Physio-
963 chemistry and optical properties, *J. Geophys. Res.*, 109, D15S09, doi:10.1029/2003JD004378,
964 2004.
- 965 Colarco, P. R., Nowottnick, E. P., Randles, C. A., Yi, B., Yang, P., Kim, K.-M., Smith, J. A., and Bar-
966 deen, C. G.: Impact of radiatively interactive dust aerosols in the NASA GEOS-5 climate model:
967 Sensitivity to dust particle shape and refractive index, *J. Geophys. Res. Atmos.*, 119, 753–786,
968 doi:10.1002/2013JD020046, 2014.
- 969 Cuesta, J., Eremenko, M., Flamant, C., Dufour, G., Laurent, B., Bergametti, G., Hopfner, M., Orphal,
970 J., and Zhou, D.: Three-dimensional distribution of a major desert dust outbreak over East Asia in
971 March 2008 derived from IASI satellite observations, *J. Geophys. Res.*, 120, 7099–7127, 2015.
- 972 Davies, C. N. : Particle-fluid interaction, *J. Aerosol. Sci.*, 10, 477–513, 1979.



- 973 Denjean, C., Cassola, F., Mazzino, A., Triquet, S., Chevaillier, S., Grand, N., Bourriane, T., Mom-
974 boisse, G., Sellegri, K., Schwarzenbock, A., Freney, E., Mallet, M., and Formenti, P.: Size distribu-
975 tion and optical properties of mineral dust aerosols transported in the western Mediterranean, *At-
976 mos. Chem. Phys.*, 16, 1081-1104, doi:10.5194/acp-16-1081-2016, 2016.
- 977 DeSouza-Machado, S. G., Strow, L. L., Hannon, S. E., and Motteler, H. E.: Infrared dust spectral sig-
978 natures from AIRS, *Geophys. Res. Lett.*, 33(L03801), 1-5, 2006.
- 979 Di Biagio, C., Boucher, H., Caquineau, S., Chevaillier, S., Cuesta, J., and Formenti, P.: Variability of
980 the infrared complex refractive index of African mineral dust: experimental estimation and implica-
981 tions for radiative transfer and satellite remote sensing, *Atmos. Chem. Phys.*, 14, 11093–11116,
982 2014a.
- 983 Di Biagio, C., P. Formenti, S. A. Styler, E. Pangui, and J.-F. Doussin: Laboratory chamber measure-
984 ments of the longwave extinction spectra and complex refractive indices of African and Asian min-
985 eral dusts, *Geophys. Res. Lett.*, 41, 6289-6297, doi:10.1002/2014GL060213, 2014b.
- 986 Di Biagio, C., P. Formenti, Y. Balkanski, L. Caponi, M. Cazaunau, E. Pangui, J.-F. Doussin, et al.:
987 Global scale variability of the mineral dust shortwave refractive index, in preparation.
- 988 di Sarra, A., Di Biagio, C., Meloni, D., Monteleone, F., Pace, G., Pugnaghi, S., and Sferlazzo, D.:
989 Shortwave and longwave radiative effects of the intense Saharan dust event of March 25-26, 2010,
990 at Lampedusa (Mediterranean sea), *J. Geophys. Res.*, 116, D23209, doi:10.1029/2011JD016238,
991 2011.
- 992 Dorschner, J., Friedemann, C., and Guertler, J.: Laboratory spectra of phyllosilicates and the interstel-
993 lar 10-micrometer absorption band, *Astron. Nachr.*, 299, 269 – 282, 1978.
- 994 Dubovik, O., Sinyuk, A., Lapyonok, T., Holben, B.N., Mishchenko, M., Yang, P., Eck, T.F., Volten,
995 H., Muñoz, O., Veihelmann, B., van der Zande, W.J., Leon, J.-F., Sorokin, M., and Slutsker, I.: Ap-
996 plication of spheroid models to account for aerosol particle nonsphericity in remote sensing of de-
997 sert dust. *J. Geophys. Res.*, 111, D11208, doi:10.1029/2005JD006619, 2006.
- 998 Dufresne, J.-L., Gautier, C., Ricchiazzi, P., and Fouquart, Y.: Longwave scattering effects of mineral
999 aerosols, *J. Atmos. Sci.*, 59, 1959–1966, 2002.
- 1000 Flores, J. M., Trainic, M., Borrmann, S., and Rudich, Y.: Effective broadband refractive index retrieval
1001 by a white light optical particle counter, *Phys. Chem. Chem. Phys.*, 11, 7943–7950, 2009.
- 1002 Formenti, P., Rajot, J. L., Desboeufs, K., Said, F., Grand, N., Chevaillier, S., and Schmechtig, C.: Air-
1003 borne observations of mineral dust over western Africa in the summer Monsoon season: spatial and
1004 vertical variability of physico-chemical and optical properties, *Atmos. Chem. Phys.*, 11, 6387-6410,
1005 doi:10.5194/acp-11-6387-2011, 2011.
- 1006 Formenti, P., Caquineau, S., Desboeufs, K., Klaver, A., Chevaillier, S., Journet, E., and Rajot, J. L.:
1007 Mapping the physico-chemical properties of mineral dust in western Africa: mineralogical composi-
1008 tion, *Atmos. Chem. Phys.*, 14, 10663-10686, doi:10.5194/acp-14-10663-2014, 2014.
- 1009 Fouquart, Y., Bonnel, B., Brogniez, G., Buriez, J. C., Smith, L., and Morcrette, J. J.: Observations of
1010 Sahara aerosols: Results of ECLATS field experiment. Part II: Broadband radiative characteristics
1011 of the aerosols and vertical radiative flux divergence, *J. Climate Appl. Meteor.*, 26, 38-52, 1987.



- 1012 Ginoux, P., Prospero, J. M., Gill, T. E., Hsu, N. C., and Zhao, M.: Global-scale attribution of anthro-
1013 pogenic and natural dust sources and their emission rates based on MODIS Deep Blue aerosol
1014 products, *Rev. Geophys.*, 50, RG3005, doi:10.1029/2012RG000388, 2012.
- 1015 Glotch, T. D., Rossman, G. R., and Aharonson, O.: Mid-infrared (5–100 μm) reflectance spectra and
1016 optical constants of ten phyllosilicate minerals, *Icarus*, 192, 604–622, 2007.
- 1017 Goudie, A. S., and Middleton, N. J.: Saharan dust storms: Nature and consequences, *Earth-Sci. Rev.*,
1018 56, 179–204, 2001.
- 1019 Goudie A. S., and Middleton, N. J.: Desert dust in the global system. Springer, Berlin, Heidelberg,
1020 New York, 2006.
- 1021 Hansell, Jr., R. A., Reid, J. S., Tsay, S. C., Roush, T. L., and Kalashnikova, O. V.: A sensitivity study
1022 on the effects of particle chemistry, asphericity and size on the mass extinction efficiency of min-
1023 eral dust in the earth's atmosphere: from the near to thermal IR, *Atmos. Chem. Phys.*, 11, 1527-
1024 1547, doi:10.5194/acp-11-1527-2011, 2011.
- 1025 Hess, M., Koepke, P., and Schult, I.: Optical properties of aerosols and clouds: The software package
1026 OPAC, *Bull. Am. Meteorol. Soc.*, 79, 831–844, 1998.
- 1027 Highwood, E. J., Haywood, J. M., Silverstone, M. D., Newman, S. M., and Taylor, J. P.: Radiative
1028 properties and direct effect of Saharan dust measured by the C-130 aircraft during Saharan Dust
1029 Experiment (SHADE): 2. Terrestrial spectrum, *J. Geophys. Res.*, 108, 8578,
1030 doi:10.1029/2002JD002552, 2003.
- 1031 Hsu, N. C., Herman, J. R., and Weaver, C. J.: Determination of radiative forcing of Saharan dust using
1032 combined TOMS and ERBE data, *J. Geophys. Res.*, 105(D16), 20,649–20,661,
1033 doi:10.1029/2000JD900150, 2000.
- 1034 Israelevich, P. L., Levin, Z., Joseph, J. H., and Ganor, E.: Desert aerosol transport in the Mediterranean
1035 region as inferred from the TOMS aerosol index, *J. Geophys. Res.*, 107 (D21), 4572,
1036 doi:10.1029/2001JD002011, 2002.
- 1037 Jeong, G. Y., Bulk and single-particle mineralogy of Asian dust and a comparison with its source soils,
1038 *J. Geophys. Res.*, 113, D02208, doi:10.1029/2007JD008606, 2008.
- 1039 Journet, E., Balkanski, Y., and Harrison, S. P.: A new data set of soil mineralogy for dust-cycle model-
1040 ing, *Atmos. Chem. Phys.*, 14, 3801-3816, doi:10.5194/acp-14-3801-2014, 2014.
- 1041 Kaaden, N., Massling, A., Schladitz, A., Müller, T., Kandler, K., Schütz, L., Weinzierl, B., Petzold, A.,
1042 Tesche, M., Leinert, S., and Wiedensohler, A.: State of Mixing, Shape Factor, Number Size Distri-
1043 bution, and Hygroscopic Growth of the Saharan Anthropogenic and Mineral Dust Aerosol at Tin-
1044 fou, Morocco, *Tellus B*, 61, 51–63, 2009.
- 1045 Karyampudi, V. M., Palm, S. P., Reagen, J. A., Fang, H., Grant, W. B., Moff, H. R., Moulin, C.,
1046 Pierce, H. F., Torres, O., Browell, E. V., and Melfi, S. H.: Validation of the Saharan dust plume
1047 conceptual model using lidar, Meteosat, and ECMWF data., *Bull. Am. Meteorol. Soc.*, 80, 1045–
1048 1075, 1999.
- 1049 Kandler, K., Schütz, L., Deutscher, C., Ebert, M., Hofmann, H., Jäckel, S., Jaenicke, R., Knippertz, P.,



- 1050 Lieke, K., Massling, A., Petzold, A., Schladitz, A., Weinzierl, B., Wiedensohler, A., Zorn, S., and
1051 Weinbruch, S.: Size distribution, mass concentration, chemical and mineralogical composition and
1052 derived optical parameters of the boundary layer aerosol at Tinfou, Morocco, during SAMUM
1053 2006, *Tellus B*, 61, 32–50, doi:10.1111/j.1600-0889.2008.00385.x, 2009.
- 1054 Kim, D., Chin, M., Yu, H., Eck, T. F., Sinyuk, A., Smirnov, A., and Holben, B.: Dust optical
1055 properties over North Africa and Arabian Peninsula derived from the AERONET dataset, *Atmos.*
1056 *Chem. Phys.*, 11, 10733–10741, doi:10.5194/acp-11-10733-2011, 2011.
- 1057 Klaver, A., Formenti, P., Caqueneau, S., Chevaillier, S., Ausset, P., Calzolari, G., Osborne, S., Johnson,
1058 B., Harrison, M., and Dubovik, O.: Physico-chemical and optical properties of Sahelian and
1059 Saharan mineral dust: in situ measurements during the GERBILS campaign, *Q. J. Roy. Meteor.*
1060 *Soc.*, 137, 1193–1210, doi:10.1002/qj.889, 2011.
- 1061 Klüser, L., Martynenko, D., and Holzer-Popp, T.: Thermal infrared remote sensing of mineral dust
1062 over land and ocean: a spectral SVD based retrieval approach for IASI, *Atmos. Meas. Tech.*, 4,
1063 757–773, 2011.
- 1064 Koepke, P., Gasteiger, J., and Hess, M.: Technical Note: Optical properties of desert aerosol with non-
1065 spherical mineral particles: data incorporated to OPAC, *Atmos. Chem. Phys.*, 15, 5947–5956,
1066 doi:10.5194/acp-15-5947-2015, 2015.
- 1067 Lafon, S., Sokolik, I. N., Rajot, J. L., Caqueneau, S., and Gaudichet, A.: Characterization of iron oxides
1068 in mineral dust aerosols: Implications for light absorption, *J. Geophys. Res.*, 111, D21207,
1069 10.1029/2005jd007016, 2006.
- 1070 Laskina, O., Young, M. A., Kleiber, P. D., and Grassian, V. H.: Infrared extinction spectra of mineral
1071 dust aerosol: single components and complex mixtures, *J. Geophys. Res.*, 117, D18210,
1072 doi:10.1029/2012JD017756, 2012.
- 1073 Legrand, M., Dubovik, O., Lapyonok, T., and Derimian, Y.: Accounting for particle non-sphericity in
1074 modeling of mineral dust radiative properties in the thermal infrared, *J. Quant. Spectros. Rad.*
1075 *Transf.*, 149, 219–240, 2014.
- 1076 Leon, J-F., and Legrand, M.: Mineral dust sources in the surroundings of the north Indian Ocean,
1077 *Geophys. Res. Lett.*, doi: 10.1029/2002GL016690, 2003.
- 1078 Lepple, F. K. and Brine, C. J.: Organic constituents in eolian dust and surface sediments from
1079 northwest Africa, *J. Geophys. Res.*, 81, 1141–1147, 1976.
- 1080 Liao, H. and Seinfeld, J. H.: Radiative forcing by mineral dust aerosols: sensitivity to key variables, *J.*
1081 *Geophys. Res.*, 103(D24), 31 637–31 646, doi:10.1029/1998JD200036, 1998.
- 1082 Long, L. L., Querry, M. R., Bell, R. J., and Alexander, R. W.: Optical properties of calcite and gypsum
1083 in crystalline and powdered form in the infrared and far-infrared, *Infrared Physics*, 34, 191–201,
1084 1993.
- 1085 Maddy, E. S., DeSouza-Machado, S. G., Nalli, N. R., Barnet, C. D., Strow, L. L., Wolf, W. W., Xie,
1086 H., Gambacorta, A., King, T. S., Joseph, E., Morris, V., Hannon, S. E., and Schou, P.: On the ef-
1087 fect of dust aerosols on AIRS and IASI operational level 2 products, *Geophys. Res. Lett.*, 39 ,
1088 L10809, doi:10.1029/2012GL052070, 2012.



- 1089 Marticorena, B., Chatenet, B., Rajot, J. L., Traoré, S., Coulibaly, M., Diallo, A., Koné, I., Maman, A.,
1090 Ndiaye, T., and Zakou, A.: Temporal variability of mineral dust concentrations over West Africa:
1091 analyses of a pluriannual monitoring from the AMMA Sahelian Dust Transect, *Atmos. Chem.*
1092 *Phys.*, 10, 8899–8915, 2010.
- 1093 Maring, H., Savoie, D. L., Izaguirre, M. A., Custals, L., and Reid, J. S.: Mineral dust aerosol size dis-
1094 tribution change during atmospheric transport, *J. Geophys. Res.*, 108, 8592,
1095 doi:10.1029/2002jd002536, 2003.
- 1096 McConnell, C. L., Formenti, P., Highwood, E. J., and Harrison, M. A. J.: Using aircraft measurements
1097 to determine the refractive index of Saharan dust during the DODO Experiments, *Atmos. Chem.*
1098 *Phys.*, 10, 3081–3098, doi:10.5194/acp-10-3081-2010, 2010.
- 1099 McMurry, P. H., and Rader, D. J.: Aerosol Wall Losses in Electrically Charged Chambers, *Aerosol*
1100 *Sci. Tech.*, 4:3, 249-268, 1985.
- 1101 Meloni, D., Junkermann, W., di Sarra, A., Cacciani, M., De Silvestri, L., Di Iorio, T., Estellés, V.,
1102 Gómez-Amo, J. L., Pace, G., and Sferlazzo, D. M.: Altitude-resolved shortwave and longwave radi-
1103 ative effects of desert dust in the Mediterranean during the GAMARF campaign: Indications of a
1104 net daily cooling in the dust layer. *J. Geophys. Res. Atmos.*, 120, 3386–3407. doi:
1105 10.1002/2014JD022312, 2015.
- 1106 Miller, R. L., Knippertz, P., Pérez García-Pando, C., Perlwitz, J. P., and Tegen, I.: Impact of dust radi-
1107 ative forcing upon climate. In *Mineral Dust: A Key Player in the Earth System*. P. Knippertz, and
1108 J.-B.W. Stuut, Eds. Springer, 327-357, doi:10.1007/978-94-017-8978-3_13, 2014.
- 1109 Osada, K., Ura, S., Kagawa, M., Mikami, M., Tanaka, T. Y., Matoba, S., Aoki, K., Shinoda, M., Kuro-
1110 saki, Y., Hayashi, M., Shimizu, A., and Uematsu, M.: Wet and dry deposition of mineral dust parti-
1111 cles in Japan: factors related to temporal variation and spatial distribution, *Atmos. Chem. Phys.*, 14,
1112 1107–1121, doi: 10.5194/acp-14-1107-2014, 2014.
- 1113 Osborne, S. R., Johnson, B. T., Haywood, J. M., Baran, A. J., Harrison, M. A. J., and McConnell, C.
1114 L.: Physical and optical properties of mineral dust aerosol during the Dust and Biomass-burning
1115 Experiment, *J. Geophys. Res.*, 113, D00C03, doi:10.1029/2007jd009551, 2008.
- 1116 Otto, S., Bierwirth, E., Weinzierl, B., Kandler, K., Esselborn, M., Tesche, M., Schladitz, A., Wendisch,
1117 M., and Trautmann, T.: Solar radiative effects of a Saharan dust plume observed during SAMUM
1118 assuming spheroidal model particles, *Tellus B*, 61, 270–296, doi:10.1111/j.1600-
1119 0889.2008.00389.x, 2009.
- 1120 Perlwitz, J. P., Pérez García-Pando, C., and Miller, R. L.: Predicting the mineral composition of dust
1121 aerosols — Part 1: Representing key processes. *Atmos. Chem. Phys.*, 15, 11593-11627,
1122 doi:10.5194/acp-15-11593-2015, 2015a.
- 1123 Perlwitz, J. P., Pérez García-Pando, C., and Miller, R. L.: Predicting the mineral composition of dust
1124 aerosols – Part 1: Representing key processes, *Atmos. Chem. Phys. Discuss.*, 15, 3493-3575,
1125 doi:10.5194/acpd-15-3493-2015, 2015b.
- 1126 Peterson, J. T., and Weinman, J. A.: Optical properties of quartz dust particles at infrared wavelengths,
1127 *Geophys. Res. Lett.*, 74, 6947-6952, 1969.



- 1128 Prospero, J. M., Ginoux, P., Torres, O., Nicholson, S. E., and Gill, T. E.: Environmental characteriza-
1129 tion of global sources of atmospheric soil dust identified with the Nimbus 7 Total Ozone Mapping
1130 Spectrometer (TOMS) absorbing aerosol product, *Rev Geophys*, 40, 1002, 2002.
- 1131 Pye, K.: *Aeolian Dust and Dust Deposits*, Academic Press, London, 334 pp., 1987.
- 1132 Querry, M.: *Optical Constants of Minerals and Other Materials from the Millimeter to the Ultraviolet*,
1133 Report CRDEC-CR-88009, US Army, Aberdeen, 1987.
- 1134 Rajot, J. L., Formenti, P., Alfaro, S., Desboeufs, K., Chevaillier, S., Chatenet, B., Gaudichet, A., Jour-
1135 net, E., Marticorena, B., Triquet, S., Maman, A., Mouget, N., and Zakou, A.: AMMA dust exper-
1136 iment: an overview of measurements performed during the dry season special observation period
1137 (SOP0) at the Banizoumbou (Niger) supersite, *J. Geophys. Res.*, 113, D00C14,
1138 doi:10.1029/2008jd009906, 2008.
- 1139 Reid, E. A., Reid, J. S., Meier, M. M., Dunlap, M. R., Cliff, S. S., Broumas, A., Perry, K., and Maring,
1140 H.: Characterization of African dust transported to Puerto Rico by individual particle and size seg-
1141 regated bulk analysis, *J. Geophys. Res.*, 108, 8591, doi:10.1029/2002jd002935, 2003.
- 1142 Reid, J. S., Reid, E. A., Walker, A., Piketh, S., Cliff, S., Mandoos, A. A., Tsay, S.-C., and Eck, T. F.:
1143 Dynamics of southwest Asian dust particle size characteristics with implications for global dust re-
1144 search, *J. Geophys. Res.*, 113, doi:10.1029/2007JD009752, 2008.
- 1145 Ryder, C. L., Highwood, E. J., Rosenberg, P. D., Trembath, J., Brooke, J. K., Bart, M., Dean, A., Cro-
1146 sier, J., Dorsey, J., Brindley, H., Banks, J., Marsham, J. H., McQuaid, J. B., Sodemann, H., and
1147 Washington, R.: Optical properties of Saharan dust aerosol and contribution from the coarse mode
1148 as measured during the Fennec 2011 aircraft campaign, *Atmos. Chem. Phys.*, 13, 303–325, 2013a.
- 1149 Ryder, C. L., Highwood, E. J., Lai, T. M., Sodemann, H., and Marsham, J. H.: Impact of atmospheric
1150 transport on the evolution of microphysical and optical properties of Saharan dust, *Geophys. Res.*
1151 *Lett.*, 40, 2433–2438, doi:10.1002/grl.50482, 2013b.
- 1152 Scanza, R. A., Mahowald, N., Ghan, S., Zender, C. S., Kok, J. F., Liu, X., Zhang, Y., and Albani, S.:
1153 Modeling dust as component minerals in the Community Atmosphere Model: development of
1154 framework and impact on radiative forcing, *Atmos. Chem. Phys.*, 15, 537–561, doi:10.5194/acp-15-
1155 537-2015, 2015.
- 1156 Scheuven, D., L. Schütz, K. Kandler, M. Ebert, and S. Weinbruch, Bulk composition of northern Af-
1157 rican dust and its source sediments - A compilation, *Earth-Sci. Rev.*, 116, 170–194, 2013.
- 1158 Schuttlefield, J. D., Cox, D. and Grassian, V. H.: An investigation of water uptake on clays minerals
1159 using ATR-FTIR spectroscopy coupled with quartz crystal microbalance measurements, *J. Ge-*
1160 *ophys. Res.*, 112, D21303, doi:10.1029/2007JD00897, 2007.
- 1161 Schütz, L., and Jaenicke, R.: Particle Number and Mass Distributions above 10^{-4} cm Radius in Sand
1162 and Aerosol of the Sahara Desert, *J. Appl. Meteorol.*, 13, 863–870, 10.1175/1520-
1163 0450(1974)013<0863:PNAMDA>2.0.CO;2, 1974.
- 1164 Schütz, L., Jaenicke, R., and Pietrek, H.: Saharan dust transport over the North Atlantic Ocean, *Geol.*
1165 *Soc. Am. Spec. Paper*, 186, 87–100, 10.1130/SPE186-p87, 1981.



- 1166 Seinfeld, J. H., and Pandis, S. N.: Atmospheric Chemistry and Physics: From Air Pollution to Climate
1167 Change, Wiley, New York, 2006.
- 1168 Sertsu, S. M., and Sánchez, P. A.: Effects of Heating on Some Changes in Soil Properties in Relation
1169 to an Ethiopian Land Management Practice, *Soil Sci. Soc. Am. J.*, 42, 940-944, 1978.
- 1170 Shen, Z. X., Li, X., Cao, J., Caquineau, S., Wang, Y., and Zhang, X.: Characteristics of clay minerals
1171 in Asian dust and their environmental significance, *China Particuology*, 3, 260–264, 2005.
- 1172 Slingo, A., Ackerman, T. P., Allan, R. P., Kassianov, E. I., McFarlane, S. A., Robinson, G. J., Barnard,
1173 J. C., Miller, M. A., Harries, J. E., Russell, J. E., and Dewitte, S.: Observations of the impact of a
1174 major Saharan dust storm on the atmospheric radiation balance, *Geophys. Res. Lett.*, 33, L24817,
1175 doi:10.1029/2006GL027869, 2006.
- 1176 Sokolik I. N., Andronova, A. V., and Jonhson, T. C.: Complex refractive index of atmospheric dust
1177 aerosols, *Atmos. Environ.*, 16, 2495–2502, 1993.
- 1178 Sokolik, I. N. and Toon, O. B.: Direct radiative forcing by anthropogenic airborne mineral aerosols,
1179 *Nature*, 381, 681–683, 1996.
- 1180 Sokolik, I. N., Toon, O. B., Bergstrom, R. W.: Modeling the radiative characteristics of airborne min-
1181 eral aerosols at infrared wavelengths, *J. Geophys. Res.*, 103 : 8813-8826, 1998.
- 1182 Sokolik, I., and Toon, O.: Incorporation of mineralogical composition into models of the radiative
1183 properties of mineral aerosol from UV to IR wavelengths, *J. Geophys. Res.*, 104(D8), 9423-9444,
1184 1999.
- 1185 Sokolik, I. N.: The spectral radiative signature of windblown mineral dust: implications for remote
1186 sensing in the thermal IR region, *Geophys. Res. Lett.*, 29, 2154, doi:10.1029/2002GL015910, 2002.
- 1187 Tegen, I. and Lacis, A. A.: Modeling of particle size distribution and its influence on the radiative
1188 properties of mineral dust aerosol, *J. Geophys. Res.*, doi: 10.1029/95JD03610, 1996.
- 1189 Toon, O. B., Pollack, J. B., and Khare, B. N.: The Optical Constants of Several Atmospheric Aerosol
1190 Species: Ammonium Sulfate, Aluminum Oxide, and Sodium Chloride, *J. Geophys. Res.*, 81, 5733–
1191 5748, 1976.
- 1192 Usher, C. R., Michel, A. E., and Grassian, V. H.: Reactions on mineral dust, *Chem. Rev.*, 103, 4883–
1193 4939, 2003.
- 1194 Vickery, K. J., Eckardt, F. D. and Bryant, R. G.: A sub-basin scale dust plume source frequency inven-
1195 tory for southern Africa, 2005–2008, *Geophys. Res. Lett.*, 40, 5274–5279, doi:10.1002/grl.50968,
1196 2013.
- 1197 Volz, F. E.: Longwave refractive index of atmospheric aerosol substances, *Appl. Optics*, 11, 755-759,
1198 1972.
- 1199 Volz, F. E.: Longwave optical constants of ammonium sulfate, Sahara dust; volcanic pumice and
1200 flyash, *Appl. Optics.*, 12, 564-568, 1973.
- 1201 von der Weiden, S.-L., Drewnick, F., and Borrmann, S.: Particle Loss Calculator – a new software tool
1202 for the assessment of the performance of aerosol inlet systems, *Atmos. Meas. Tech.*, 2, 479–494,
1203 2009.



- 1204 Wang, J., Doussin, J. F., Perrier, S., Perraudin, E., Katrib, Y., Pangu, E., and Picquet-Varrault, B.:
1205 Design of a new multi-phase experimental simulation chamber for atmospheric photo-smog, aerosol
1206 and cloud chemistry research, *Atmos. Meas. Tech.*, 4, 2465–2494, 2011.
- 1207 Washington, R., Todd, M. C., Middleton, N., Goudie, A. S.: Dust-storm source areas determined by
1208 the Total Ozone Monitoring Spectrometer and surface observations, *Ann. Assoc. Am. Geogr.*, 93,
1209 297–313, 2003.
- 1210 Weinzierl, B., Petzold, A., Esselborn, M., Wirth, M., Rasp, K., Kandler, K., Schutz, L., Koepke, P.,
1211 and Fiebig, M.: Airborne measurements of dust layer properties, particle size distribution and mix-
1212 ing state of Saharan dust during SAMUM 2006, *Tellus*, 61B, 96–117, doi:10.1111/j.1600-
1213 0889.2008.00392.x, 2009.
- 1214 White, J. U.: Long optical path of large aperture, *J. Opt. Soc. Am.*, 32, 285–288, 1942.
- 1215
1216
1217
1218
1219
1220
1221
1222
1223
1224
1225
1226
1227
1228
1229
1230
1231
1232
1233
1234
1235
1236
1237
1238
1239
1240
1241
1242



1243 **Tables**

1244 **Table 1.** Measured and retrieved quantities and their estimated uncertainties. For further details refer
 1245 to Sect. 2.

1246

	Parameter	Uncertainty	Uncertainty calculation
Optical LW	Transmission 2-16 μm , T	<10%	Quadratic combination of noise (~1%) and standard deviation over 10-min (5-10%)
	Extinction coefficient 2-16 μm , $\beta_{\text{ext}}(\lambda) = \frac{-\ln(T(\lambda))}{x}$	~10%	Error propagation formula ¹ considering uncertainties on the measured transmission T and the optical path x (~2%)
Size distribution	SMPS geometrical diameter (D_g), $D_g = D_m / \chi$	~6%	Error propagation formula ¹ considering the uncertainty on the estimated shape factor χ (~6%)
	SkyGrimm geometrical diameter (D_g)	<15.2%	Standard deviation of the D_g values obtained for different refractive indices values used in the optical to geometrical conversion
	WELAS geometrical diameter (D_g)	~5-7%	The same as for the SkyGrimm
	$\left[\frac{dN}{d \log D_g} \right]_{\text{Corr, WELAS}} = \left[\frac{dN}{d \log D_g} \right] / \left[1 - L_{\text{WELAS}}(D_g) \right]$	~20-70%	Error propagation formula ¹ considering the $dN/d \log D_g$ st. dev. over 10-min and the uncertainty on L_{WELAS} (~50% at 2 μm , ~10% at 8 μm)
	$\left[\frac{dN}{d \log D_g} \right]_{\text{filter}} = \left[\frac{dN}{d \log D_g} \right]_{\text{CESAM}} * \left[1 - L_{\text{filter}}(D_g) \right]$	~25-70%	Error propagation formula ¹ considering the uncertainties on $(dN/d \log D_g)_{\text{CESAM}}$ and L_{filter} (~55% at 2 μm , ~10% at 12 μm)
Mineralogical composition	Clays mass ($m_{\text{clay}} = M_{\text{total}} - m_Q - m_F - m_C - m_D - m_G$)	8-26%	Error propagation formula ¹ considering the uncertainty on M_{total} (4-18%) and that on m_Q , m_F , m_C , m_D , and m_G
	Quartz mass ($m_Q = S_Q / K_Q$)	9%	Error propagation formula ¹ considering the uncertainty on the DRX surface area S_Q (~2%) and K_Q (9.4%)
	Feldspars mass ($m_F = S_F / K_F$)	14% (orthose), 8% (albite)	The same as for the quartz, K_F uncertainty 13.6% (orthose) and 8.4% (albite)
	Calcite mass ($m_C = S_C / K_C$)	11%	The same as for the quartz, K_C uncertainty 10.6%
	Dolomite mass ($m_D = S_D / K_D$)	10%	The same as for the quartz, K_D uncertainty 9.4%
	Gypsum mass ($m_G = S_G / K_G$)	18%	The same as for the quartz, K_G uncertainty 17.9%

1247 ¹ $\sigma_f = \sqrt{\sum_{i=1}^n \left(\frac{\partial f}{\partial x_i} \sigma_{x_i} \right)^2}$



1248 **Table 2.** Summary of information on the soil samples used in this study.

1249

1250

Sample name	Collection Coordinates	Geographical zone	Country	Desert zone
Tunisia	33.02°N, 10.67°E	Northern Africa	Tunisia	Saharan desert (Maouana)
Morocco	31.97°N, 3.28°W	Northern Africa	Morocco	Saharan desert (east of Ksar Sahli)
Libya	27.01°N, 14.50°E	Northern Africa	Libya	Sahara desert (Sebha)
Algeria	23.95°N, 5.47°E	Northern Africa	Algeria	Saharan desert (Ti-n-Tekraouit)
Mauritania	20.16°N, 12.33°W	Northern Africa	Mauritania	Saharan desert (east of Aouinet Nchir)
Niger	13.52°N, 2.63°E	Sahel	Niger	Sahel (Banizoumbou)
Mali	17.62°N, 4.29°W	Sahel	Mali	Sahel (Dar el Beida)
Bodélé	17.23°N, 19.03°E	Sahel	Chad	Bodélé depression
Ethiopia	7.50°N, 38.65°E	Eastern Africa and the Middle East	Ethiopia	Lake Shala National Park
Saudi Arabia	27.49°N, 41.98°E	Eastern Africa and the Middle East	Saudi Arabia	Nefud desert
Kuwait	29.42°N, 47.69°E	Eastern Africa and the Middle East	Kuwait	Kuwaiti desert
Gobi	39.43°N, 105.67°E	Eastern Asia	China	Gobi desert
Taklimakan	41.83°N, 85.88°E	Eastern Asia	China	Taklimakan desert
Arizona	33.15 °N, 112.08°W	North America	Arizona	Sonoran desert
Atacama	23.72°S, 70.40°W	South America	Chile	Atacama desert
Patagonia	50.26°S, 71.50°W	South America	Argentina	Patagonian desert
Namib-1	21.24°S, 14.99°E	Southern Africa	Namibia	Namib desert (area between the Kuiseb and Ugab valleys)
Namib-2	19.0°S, 13.0°E	Southern Africa	Namibia	Namib desert (Damaraland, rocky area in north-western Namibia)
Australia	31.33°S, 140.33°E	Australia	Australia	Strzelecki Desert

1251

1252



1253 **Table 3.** Position of LW absorption band peaks (6-16 μm) for the main minerals composing dust.
1254 Montmorillonite is taken here as representative for the smectite family. For feldspars literature data are
1255 available only for albite.

1256
1257

Mineral species	Wavelength (μm)	Reference
Illite	9.6	Querry (1987)
Kaolinite	9.0, 9.6, 9.9, 10.9	Glotch et al. (2007)
Montmorillonite	9.0, 9.6	Glotch et al. (2007)
Chlorite	10.2	Dorschner et al. (1978)
Quartz	9.2, 12.5-12.9	Peterson and Weinman (1969)
Calcite	7.0, 11.4	Long et al. (1993)
Gypsum	8.8	Long et al. (1993)
Albite	8.7, 9.1, 9.6	Laskina et al. (2012)

1258
1259
1260
1261
1262
1263
1264
1265
1266
1267
1268
1269
1270
1271
1272
1273

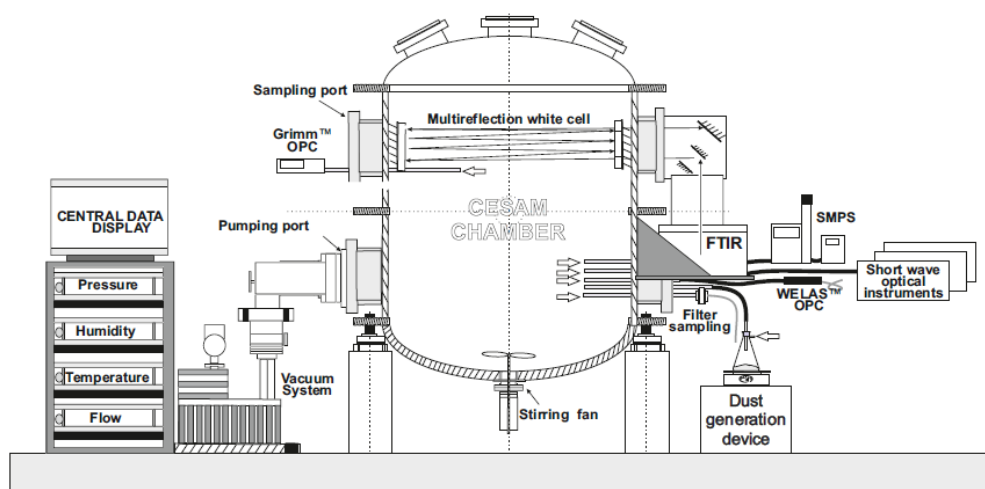


1274 **Figures**

1275

1276 **Figure 1.** Schematic configuration of the CESAM set up for the dust experiments. The dust generation
1277 (vibrating plate, Büchner flask containing the soil sample) and injection system is shown in the bottom
1278 on the right side. The position of the SMPS, WELAS, and SkyGrimm used for measuring the size distri-
1279 bution, FTIR spectrometer, SW optical instruments, and filter sampling system are also indicated.

1280



1281

1282

1283

1284

1285

1286

1287

1288

1289

1290

1291

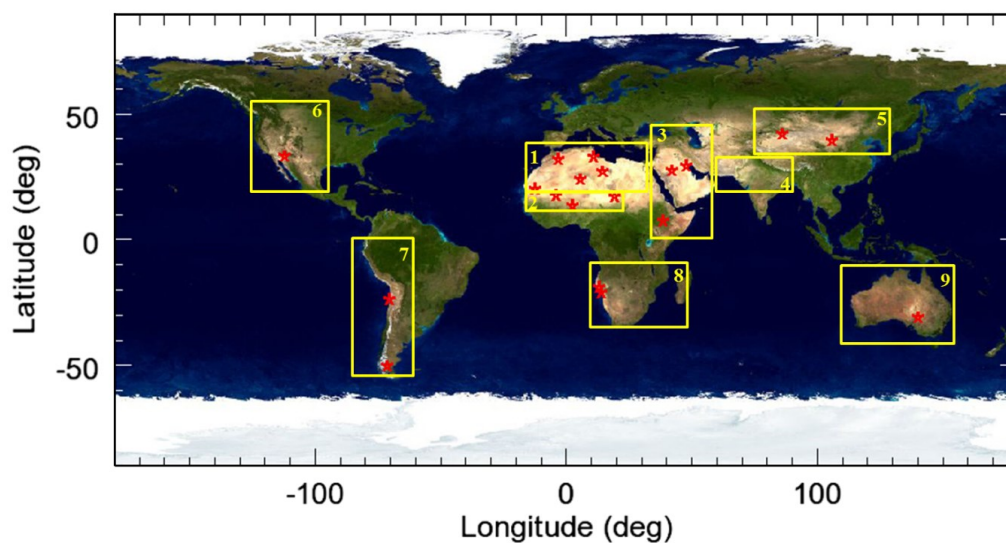
1292

1293

1294



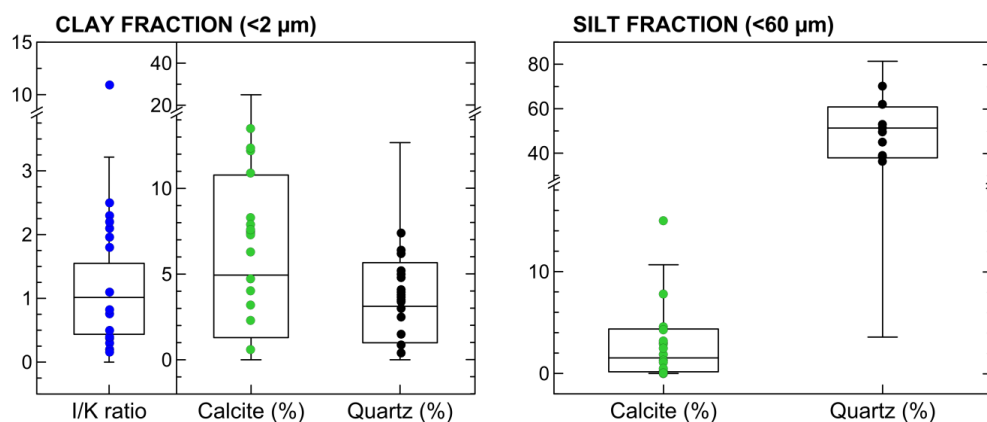
1295 **Figure 2.** Location (red stars) of the soil and sediment samples used to generate dust aerosols. The
1296 nine yellow rectangles depict the different global dust source areas as defined in Ginoux et al. (2012):
1297 1) Northern Africa, 2) Sahel, 3) Eastern Africa and Middle East, 4) Central Asia, 5) Eastern Asia,
1298 North America, 6) South America, 7) Southern Africa, and 9) Australia.
1299
1300



1301
1302
1303
1304
1305
1306
1307
1308
1309
1310
1311
1312
1313
1314
1315



1316 **Figure 3.** Box and whisker plots showing the variability of the soil composition in the clay and silt
1317 fractions at the global scale, i.e., by considering all data from the nine dust source areas identified in
1318 Fig. 2. Data are from the soil mineralogical database by Journet et al. (2014). Dots indicate specific
1319 mineralogical characteristics (illite-to-kaolinite mass ratio, I/K, calcite and quartz contents, extracted
1320 from Journet et al.) of the soils used in the CESAM experiments, as listed in Table 2.
1321
1322

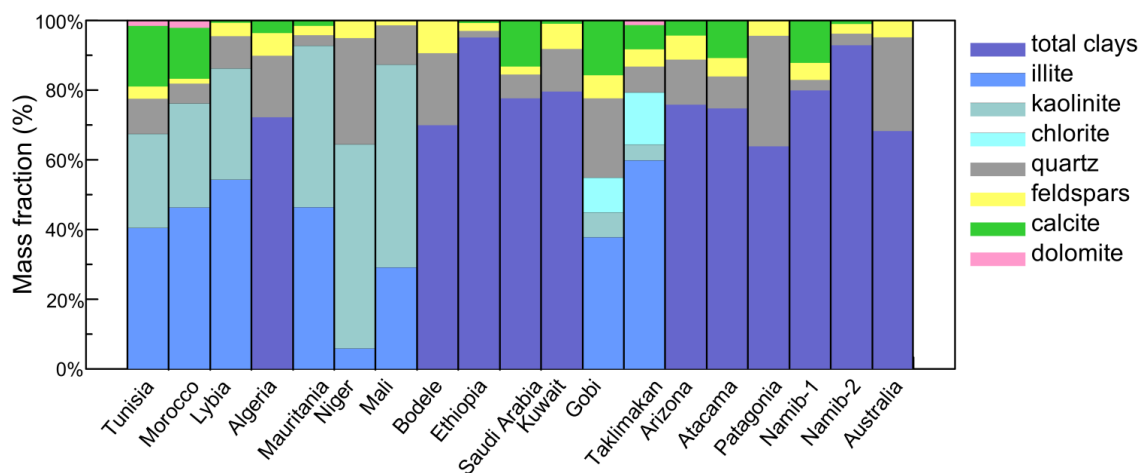


1323
1324
1325
1326
1327
1328
1329
1330
1331
1332
1333
1334
1335
1336
1337
1338
1339



1340 **Figure 4.** Mineralogy of the nineteen generated aerosol samples considered in this study, as obtained
 1341 from XRD analysis. The mass apportionment between the different clay species (illite, kaolinite, chlo-
 1342 rite) is shown for Northern African (Tunisia, Morocco, Libya, Mauritania, Niger, Mali, Bodélé) and
 1343 Eastern Asian (Gobi, Taklimakan) aerosols based on literature compiled values of the illite-to-kaolinite
 1344 (I/K) and chlorite-to-kaolinite (Ch/I) mass ratios (Scheuven et al., 2013; Formenti et al. 2014). For all
 1345 the other samples only the total clay mass is reported.

1346
 1347

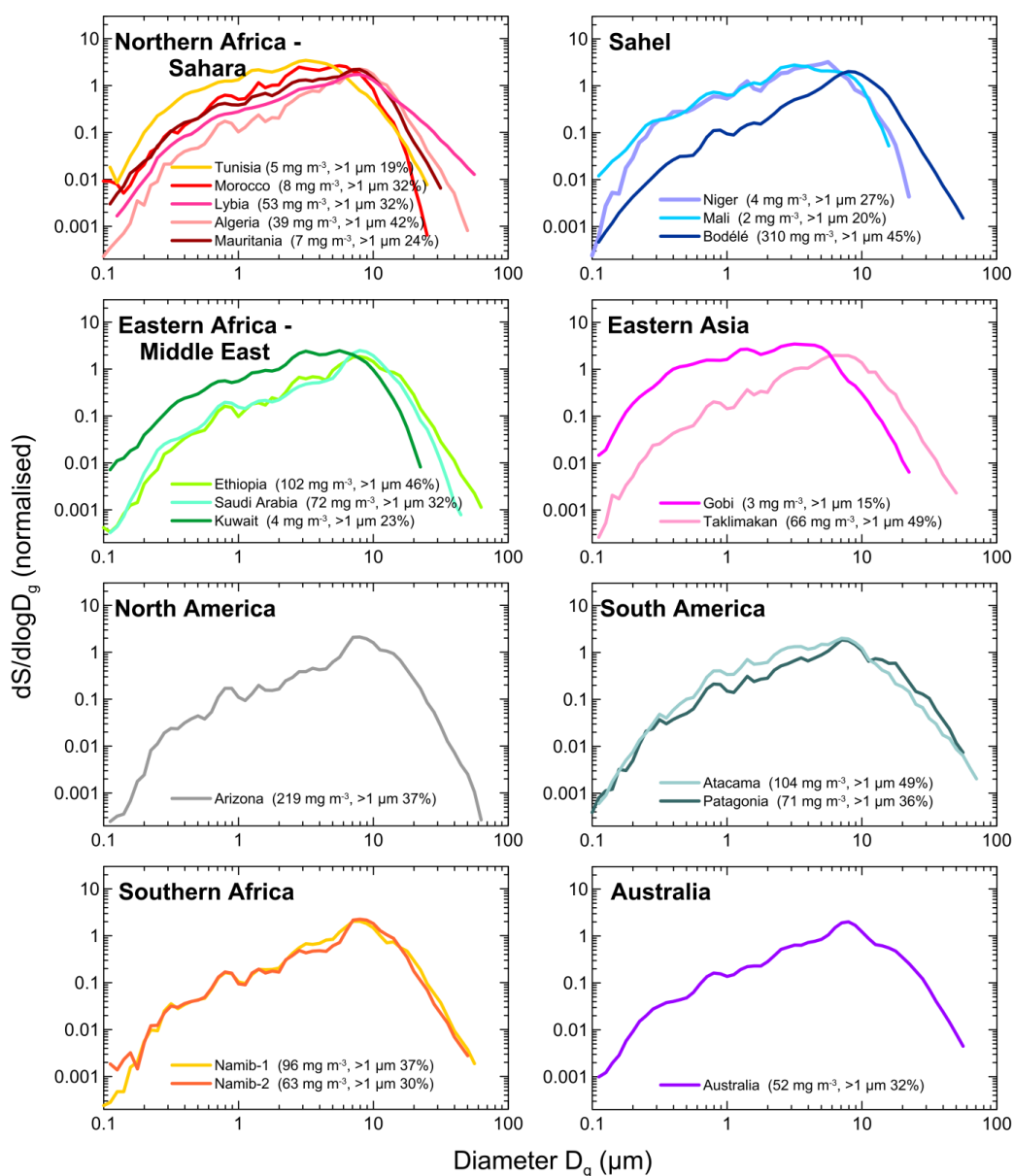


1348
 1349
 1350
 1351
 1352
 1353
 1354
 1355
 1356
 1357
 1358
 1359
 1360
 1361
 1362
 1363
 1364
 1365
 1366



1367 **Figure 5.** Surface size distributions in the CESAM chamber at the peak of dust injection for all cases
 1368 analysed in this study; the total measured dust mass concentration and the percentage of the super-
 1369 micron to sub-micron number fraction at the peak are also reported in the legend.

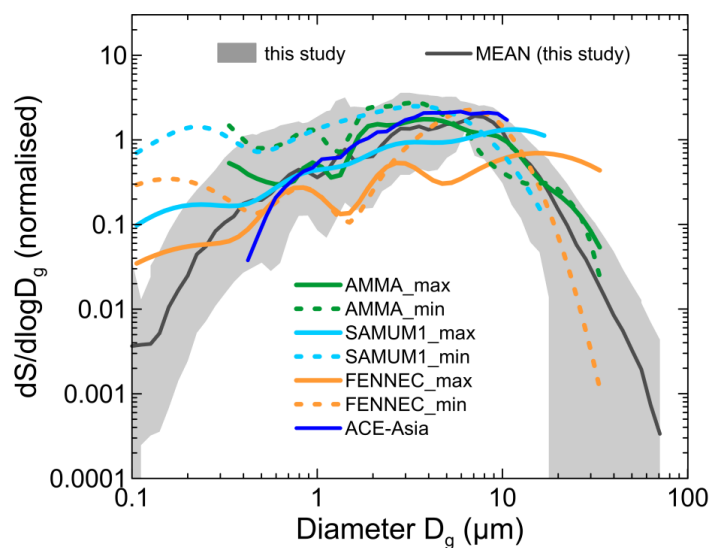
1370
 1371



1372
 1373



1374 **Figure 6.** Comparison of CESAM measurements with dust size distributions from several airborne
1375 field campaigns in Africa and Asia. The grey shaded area represents the range of sizes measured in
1376 CESAM during experiments with the different samples. Data from field campaigns are: AMMA (For-
1377 menti et al., 2011), SAMUM-1 (Weinzierl et al., 2009), FENNEC (Ryder et al., 2013a), and ACE-Asia
1378 (Clarke et al., 2004). Min and max for the same data correspond to the range of variability observed
1379 for the campaigns considered.
1380
1381

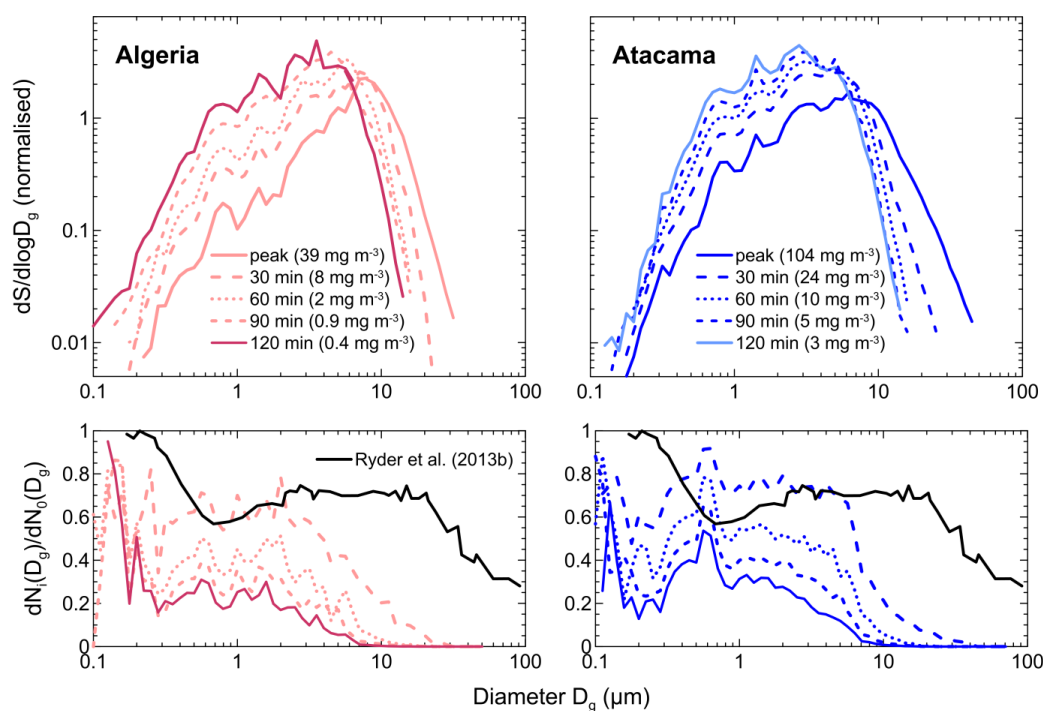


1382
1383
1384
1385
1386
1387
1388
1389
1390
1391
1392
1393
1394



1395 **Figure 7.** Upper panel: surface size distribution measured at the peak of the dust injection and at 30,
1396 60, 90, and 120 minutes after injection for Algeria and Atacama aerosols. The dust mass concentration
1397 is also indicated in the plot. Lower panel: fraction of particles remaining airborne in the chamber as a
1398 function of time versus particle size calculated as $dN_i(D_g)/dN_0(D_g)$, where $dN_i(D_g)$ is the number of
1399 particles measured by size class at the i -time (i corresponding to 30, 60, 90 and 120 min after injection)
1400 and $dN_0(D_g)$ represents the size-dependent particle number at the peak of the injection. Values are
1401 compared to the estimate of Ryder et al. (2013b) for Saharan dust layers aged 1-2 days after emission.

1402
1403

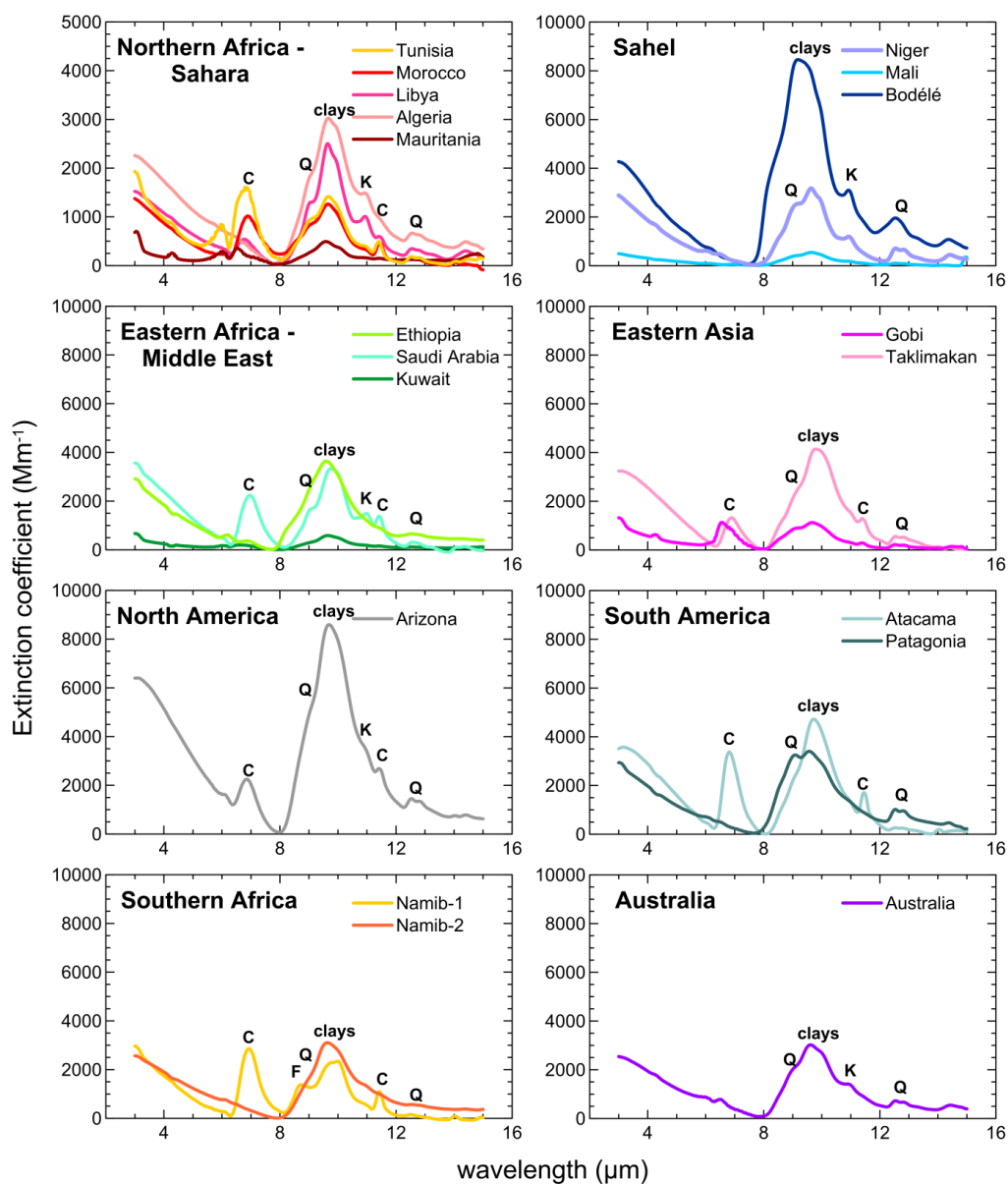


1404
1405
1406
1407
1408
1409
1410
1411
1412
1413
1414
1415



1416 **Figure 8.** Dust extinction coefficient measured in the LW spectral range for the nineteen aerosol sam-
 1417 ples analysed in this study. Data for each soil refer to the peak of the dust injection in the chamber.
 1418 Note that the y-scale is different for Northern Africa – Sahara compared to the other cases. Main ab-
 1419 sorption bands by clays at 9.6 μm , quartz (Q) at 9.2 and 12.5-12.9 μm , kaolinite (K) at 10.9 μm , calcite
 1420 (C) at 7.0 and 11.4 μm , and feldspars (F) at 8.7 μm are also indicated in the spectra.

1421



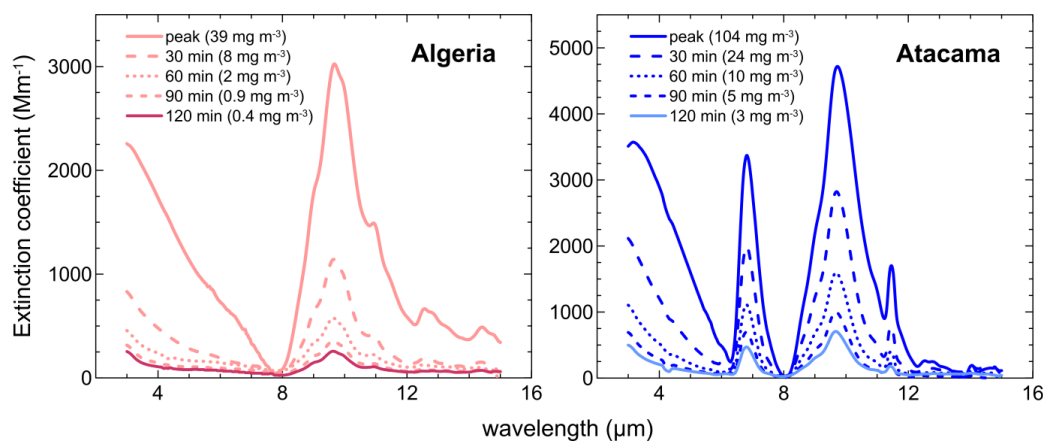
1422



1423 **Figure 9.** Extinction spectra measured at the peak of the dust injection and at 30, 60, 90, and 120
1424 minutes after injection for Algeria and Atacama aerosols.

1425

1426



1427

1428

1429

1430

1431

1432

1433

1434

1435

1436

1437

1438

1439

1440

1441

1442

1443

1444

1445

1446

1447

1448

1449

1450

1451

1452

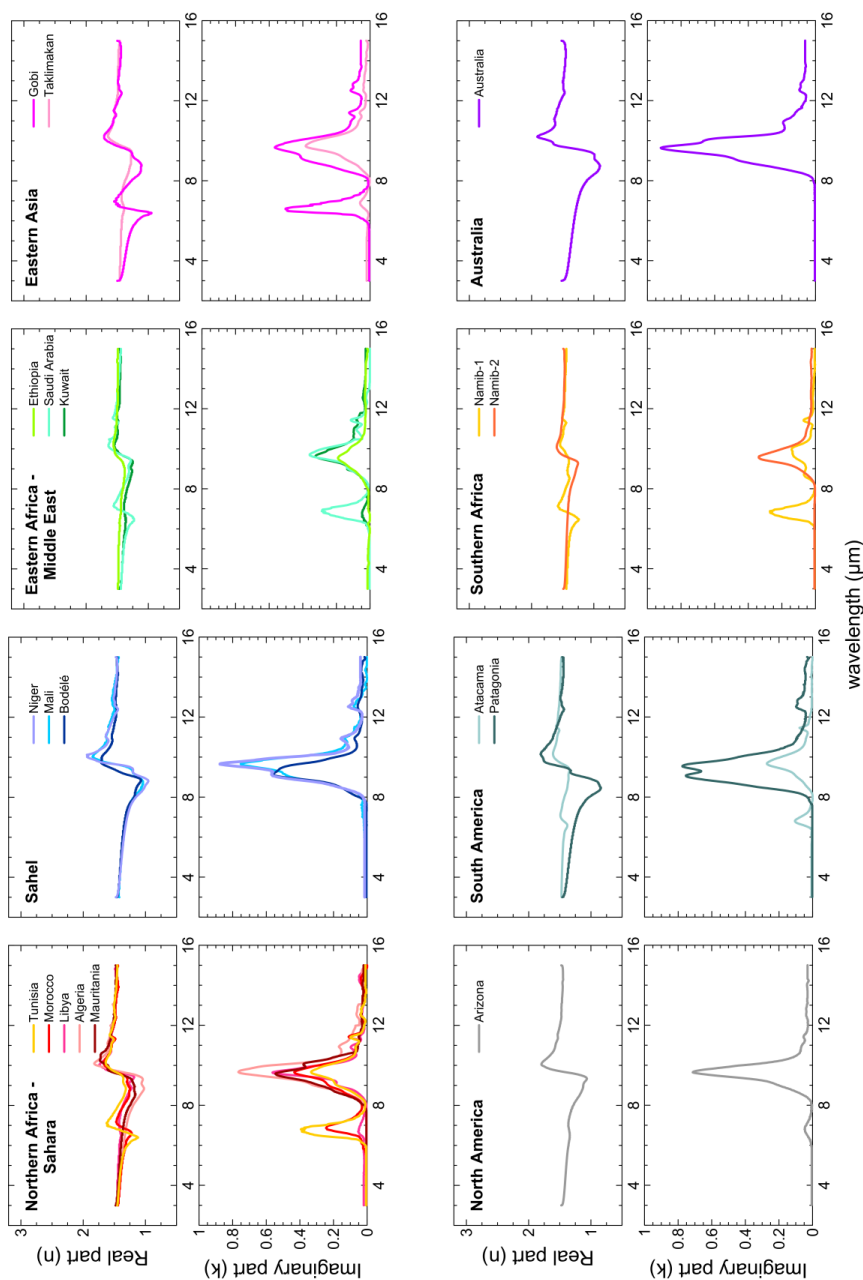
1453

1454



1455 **Figure 10.** Real (n) and imaginary (k) parts of the dust complex refractive index obtained for the nine-
 1456 teen aerosol samples analysed in this study. Data correspond to the time average of the 10-min values
 1457 obtained between the peak of the injection and 120 min later.

1458
 1459



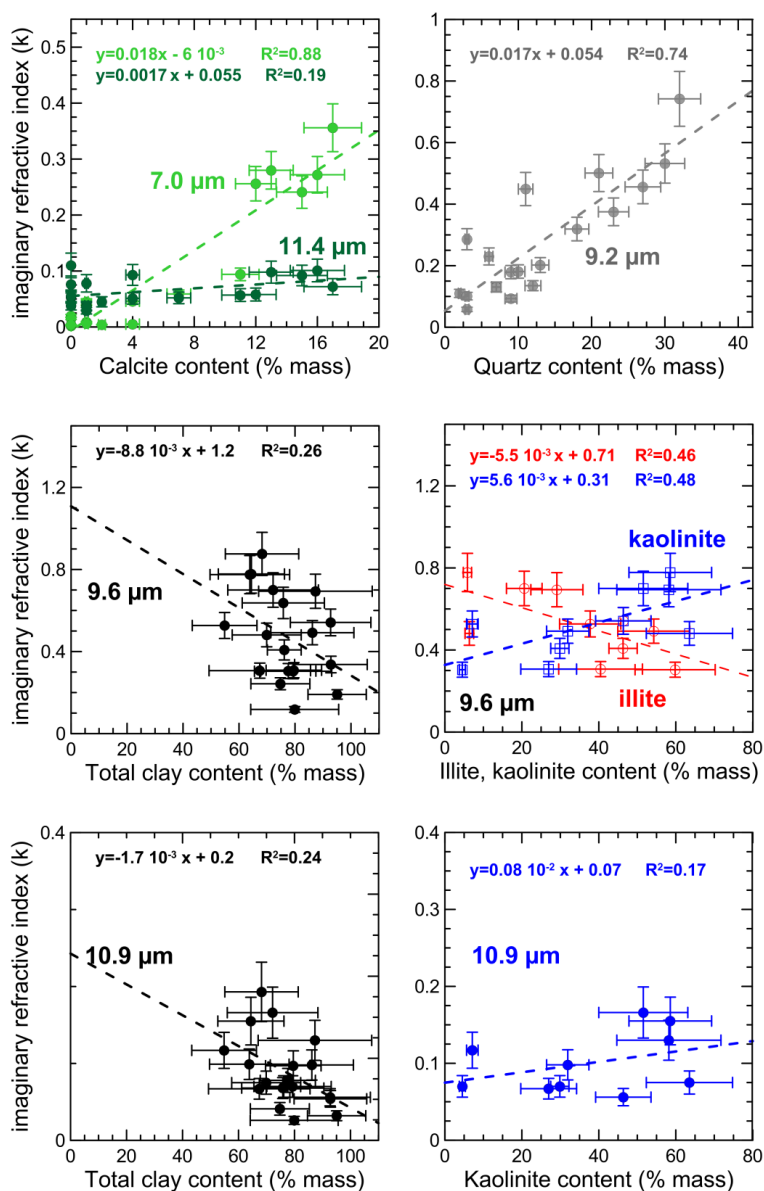
0974



1461 **Figure 11.** Imaginary part of the complex refractive index (k) versus the mineral content (in % mass)
 1462 for the bands of calcite (7.0 and 11.4 μm), quartz (9.2 μm), and clays (9.6 and 10.9 μm). For the band
 1463 at 9.6 μm the plot is drawn separately for total clays, and illite and kaolinite species. The linear fits are
 1464 also reported for each plot.

1465

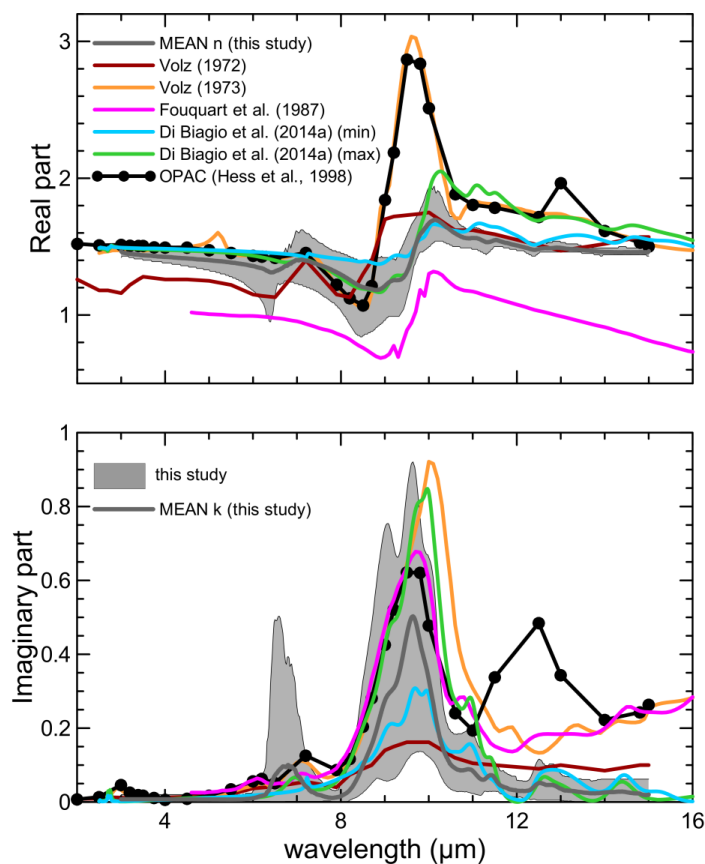
1466



1467
 1468



1469 **Figure 12.** Comparison of results obtained in this study with literature values of the dust refractive
1470 index in the LW. Literature values are taken from Volz (1972) for rainout dust collected in Germany,
1471 Volz (1973) for dust collected at Barbados, Fouquart (1987) for Niger sand, Di Biagio et al (2014a) for
1472 dust from Niger and Algeria, and the OPAC database (Hess et al., 1998). The region in gray in the plot
1473 indicates the full range of variability obtained in this study, and the dashed line is the mean of n and k
1474 obtained for the different aerosol samples. The legend in the top panel identifies the line styles used in
1475 the plot for the literature data.
1476
1477
1478

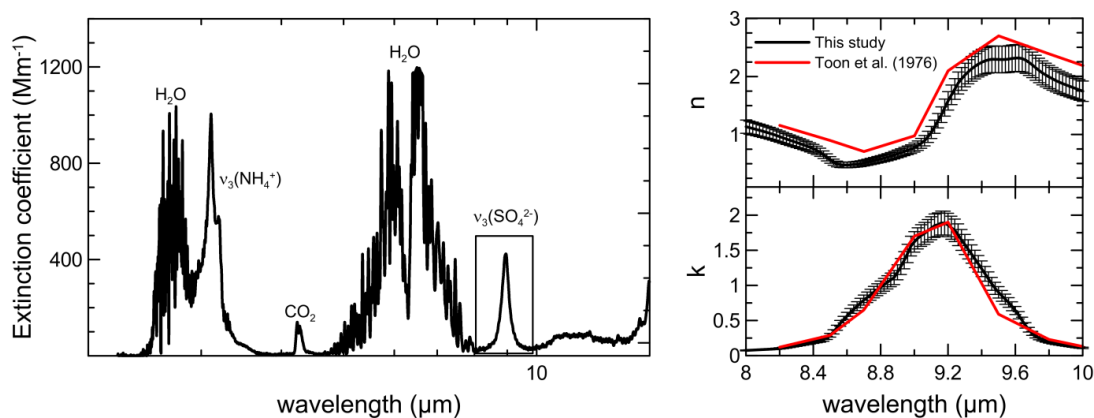


1479
1480
1481
1482
1483



1484 **Figure A1.** Left panel: longwave spectrum of ammonium sulfate measured in CESAM in the 2-15 μm
1485 range. The vibrational modes $\nu_3(\text{NH}_4^+)$ (3230 cm^{-1} or $3.10\ \mu\text{m}$) and $\nu_3(\text{SO}_4^{2-})$ (1117 cm^{-1} or 8.95
1486 μm) of ammonium sulfate are identified in the plot. Absorption bands attributed to gas-phase water
1487 vapor and CO_2 present in the chamber during experiments are also indicated. The rectangle in the plot
1488 indicates the spectral region where the retrieval of the complex refractive index was performed. Right
1489 panel: real and imaginary parts of the refractive index obtained by optical closure. The results are
1490 compared with the ammonium sulfate optical constants from Toon et al. (1976).

1491
1492
1493



1494
1495
1496
1497
1498